CMOS MEMS Resonant Mixer-Filters

by
Janet Stillman

Master's Project Report

in

Electrical Engineering

at

Carnegie Mellon University

Advisor:
Professor Gary Fedder
Second Reader:
Dr. Tamal Mukherjee

July, 2003

Abstract

This research expands the technology developed for electromechanical filters to CMOS MEMS mixer-filters. Simple mixer-filters composed of coupled CMOS MEMS resonators mix, downconvert and filter electronic inputs. The devices apply the CMOS MEMS advantages of integration of mechanical structures with CMOS circuits and multiple conductive layers on a single released structure to the growing field of MEMS signal processors.

A model is developed for the mixing and filtering functions of electrostatically actuated, laterally moving CMOS MEMS structures, with a brief discussion of their spectral response and distortion products. Mechanisms for coupling multiple resonators to form arbitrary filter shapes are discussed, including mechanical spring coupling, parallel operation, cascading resonators with different center frequencies, and electrostatic coupling. An integrated CMOS circuit and the effects of its input impedance on the frequency response are discussed.

Topologies for very simple CMOS MEMS resonators based on laterally vibrating beams are explored. A design which cuts down on feedthrough from the drive electrode to the sense electrode by separating the electrodes by several microns on a square attached to the end of the cantilever beam is presented. A model for the shape function and frequency response of this resonator matches finite element simulation closely. Tuning mechanisms, including traditional electrostatic spring softening and introducing axial-tension electrostatic spring softening, are compared. Guidelines for resonator design in CMOS include curl matching to accommodate vertical residual stress gradients, inclusion of etch holes and open areas for releasing high aspect ratio structures, and minimizing the effects of mask misalignment. Optimum sizing of a CMOS MEMS resonator is extremely application-dependent, but for the cantilever with an electrode square, larger, stiffer resonators are better because of a higher maximum polarizing voltage and superior robustness to process variations and voltage noise.

Fabricated devices are tested on a custom printed circuit board in vacuum. A bandpass filter composed of two resonators has a stopband rejection of 28 dB, a center frequency of 398.5 kHz, a ripple of 37%, and a Q of 1,533 when operated at 8 μTorr with a 23-V polarizing voltage. Mixing, downconverting resonators demonstrate Qs of more than 3000 at 8 μTorr with input frequencies of 15 MHz and 15.4 MHz and input magnitudes of 1 V.

Fixed-fixed 119 μm x 1 μm x 5 μm beams demonstrated crippling residual compressive stress, which brought the resonance frequency to 5 Hz from the stress-free resonance frequency of 362 kHz. Additional higher-order filters and alternate topologies are fabricated but not yet tested.

1 Introduction to MEMS mixer-filters

The expanding field of microelectromechanical systems (MEMS) offers advances in many fields, of which RF front end components are one of the most immediately promising. In the drive for ever smaller, lighter, cheaper, more portable and lower power radio devices, MEMS components may provide the technological breakthrough to make truly ubiquitous, convenient wireless devices possible. The availability of superior front end components would also improve many currently available radio devices such as cell phones, pagers and wireless PDAs.

One of the current limitations to portable radio frequency (RF) devices, which commonly need high accuracy channel-selecting bandpass filters, is the use of external resistors, capacitors, inductors or crystal or surface acoustic wave (SAW) resonators for the bandpass filter. These external components are both costly and large. In addition, during assembly they must be individually mounted into the system and connected to the appropriate system terminals, adding to the overall complexity of the system. The external SAW and piezoelectric ceramic resonators frequently used in cell phones and other mobile devices consume power the system can ill afford. MEMS RF devices promise solutions to some of these problems: they are small, ideally integrated right onto a system-on-a-chip, a great improvement both in assembly and area; and they use virtually no power.

The first generation of MEMS filters has already arrived on the market and is comparable to the most state-of-the-art traditional SAW filter. NEC's new three-band SAW filters (two filters at 800MHz and another at 1.5GHz for Japanese PDC mobile phones) packaged in hollow plastic packages to keep them as small and light as possible, at 3 mm x 3 mm in area, weighs in at 18 mg [1]. A new MEMS film bulk acoustic resonator (FBAR) alternative now commercially available from Agilent Technologies [2] provides similar performance: the equivalent of the two SAW filters used in a typical US CDMA mobile phones for the bands 1850-1880 MHz and 1880-1910 MHz in a 3 mm x 3 mm package.

Current research on MEMS resonators has much more ambitious goals for bandpass filters: if they can be integrated on-chip, both their area and their power consumption are negligible. Their

electrical characteristics also tend to be more ambitious than current filters: the stopband rejection is higher, the passband attenuation is less, the aging and temperature stability are superior. For example, successfully-fabricated MEMS medium frequency (340 kHz) bandpass filters use areas of about 700 μm x 200 μm [3]. Higher frequency filters will be even smaller, with GHz filter areas measured in microns or nanometers and mass in picograms [4].

Of particular interest in this thesis are down-conversion mixer-filters. In a great many modern communication systems the transmitted signal is up-converted to a carrier frequency well above the data rate. In a traditional superheterodyne receiver this received high-frequency signal is amplified, passed through an RF bandpass filter and then mixed with a local oscillator whose frequency puts the mixed output in an intermediate frequency band where a set of IF bandpass filters select the desired channel. These RF and IF bandpass filters tend to be costly in area and power consumption. In contrast, MEMS-based mixer-filters can mix the input with a local oscillator at the carrier frequency so the mixed result is downconverted and filtered at the IF immediately. This architecture, which is the target system for the MEMS mixer-filters described in this thesis, is more power-efficient. This is because there are fewer high-frequency stages and because driving the high impedance MEMS mixer-filter loads requires less power than driving high-quality low-impedance passive filters [5]. The MEMS devices are also much smaller in area than their alternatives. An array of many mixer-filters can monitor many frequency bands in parallel in a relatively small area, a capability that could revolutionize transceiver architectures.

The MEMS mixer-filters of this work consist of electrostatically actuated mechanically resonant structures with electrical outputs fabricated in a standard CMOS process. They can be integrated into the same CMOS die as the rest of the radio and digital circuitry. They are post-processed with a few maskless micromachining steps—which are fully compatible with the CMOS circuitry— to release the MEMS structures [6]. This Carnegie Mellon CMOS MEMS process uses metal layers from the CMOS process, obtained through MOSIS, to mask the desired mechanical structures and cover the circuitry. A silicon-dioxide-selective anisotropic reactive ion etch (RIE) removes the dielectric in the areas not masked by a metal layer. A subsequent anisotropic silicon RIE etch removes the silicon in the unprotected areas. A final isotropic silicon etch undercuts a few microns of the silicon beneath the masked areas as well. The resonators are therefore composed of the selected CMOS aluminum layers and any of the dielectric between and below them, as shown in Figure 1-1 below, taken from [6].

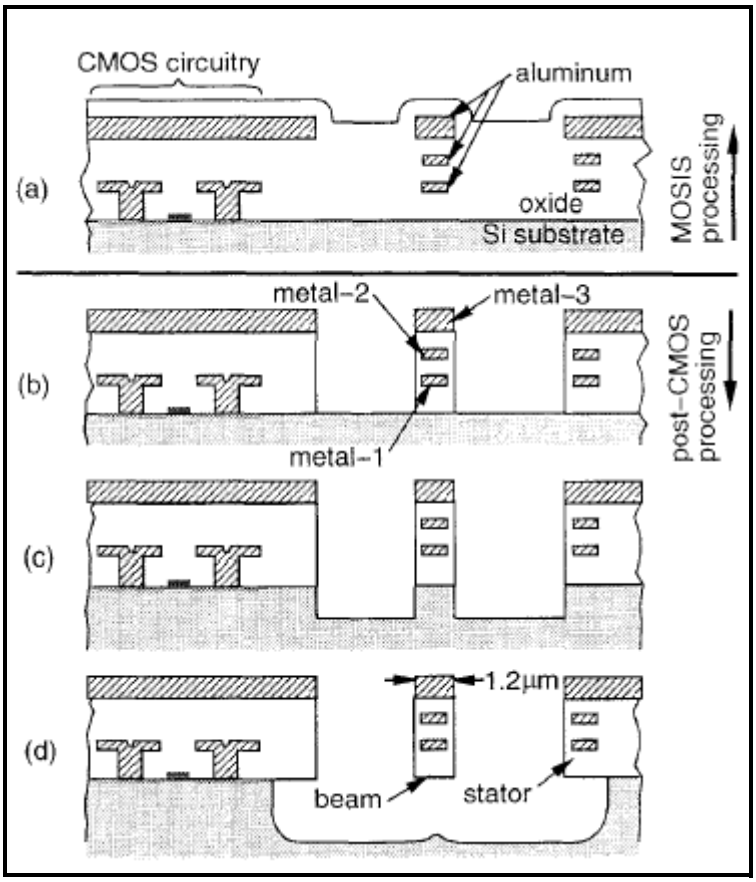

Figure 1-1. Steps to create CMOS MEMS. The fabrication starts with a), a CMOS die purchased through MOSIS, containing both CMOS circuitry covered by a top metal layer to protect it from etching and areas which will become mechanical structures. b) An oxide-selective RIE removes all the material down to the substrate, except areas under metal. c) A silicon RIE removes a small amount of silicon in the exposed areas and d) a final etch undercuts the silicon a short distance in every direction, releasing the MEMS structures.

MEMS bandpass filters and mixer-filters are not new. Filters composed of multiple MEMS resonators with superior ripple than achieved here have been repeatedly demonstrated in other processes. The stopband rejection and linearity of some of the previously-reported devices are also superior to what has been achieved here [3],[9],[11],[14]. The contributions of this thesis are to apply the already-established guidelines for designing MEMS resonators, bandpass filters, and mixers to CMOS MEMS, which has unique limitations and promise; and to explore and compare alternative coupling topologies for extending the cascading of MEMS bandpass filters. Fabrication of a variety of single resonators with resonant frequencies from 340 kHz to 10 MHz explore the manufacturability, sensitivity and quality factors of the selected topologies. Additional blocks cascade two or three resonators together to provide a wider bandpass with a smaller ripple, attempting to achieve a Chebyshev polynomial filter. Several coupling schemes are evaluated: small physical springs and a few electrostatic coupling mechanisms. To improve the sensitivity and signal to noise ratio, groups of resonators actuated and sensed in parallel were ganged together.

The design goals for the bandpass filters are set to practical values, for eventual integration into a frequency-hopping communications system. With that target application in mind, the RF and LO input frequencies the filters must handle should range from a few MHz to 2.5 GHz. These inputs will be driven by other blocks on the same chip, so at these higher frequencies distortion considerations will limit their amplitudes: the filters should respond adequately to input AC amplitudes of

about .75 V. The target filter bandwidth is 10 kHz. The center frequencies for this system range from 1 MHz to 6 MHz. The stopband rejection should be no less than 40 dB and preferably the 60 dB of current commercial cell-phone band select filters. The output voltage magnitude, including any integrated electronics, should also be in the general range of .75 V. The ripple should be no more than ten percent; however for this first exploration of filters the number of resonators cascaded together has not been pushed beyond three, so either the actual ripple or conversion loss may be sacrificed. The electrostatic transduction process introduces intermodulation distortion, which should be limited to -20 dB or less . The design and fabrication should be fairly insensitive to process variation; in practice, this is impossible to achieve at sub-micron dimensions, so dynamic tuning to bring the resonator and coupling mechanism back to the desired values must be included in the design of each filter.

At this stage of design, signal distribution has not been modeled or included as a consideration. It is assumed that the previous stages of the system can drive the high-impedance loads the filters present without excessive reflections.

There are two immediate goals of this research. The first is to show that CMOS MEMS offers the potential to make excellent, mass-produced signal processing elements which can easily be integrated onto the same chip as extensive CMOS circuitry. The second is to compare schemes for coupling multiple CMOS resonators together for a low-ripple, low conversion-loss MEMS mixer-filter.

2 Mixer-filter design and modeling

Electromechanical filter design draws from a history of robust, well-researched macro scale devices. Electromechanical filters have been used since the 1940s and continue to be selected over purely electronic filters under some circumstances for their narrow bandwidth, extremely high quality factor, good aging and temperature stability, and low insertion loss [10]. In the last 40 years, attempts to fabricate similar electromechanical filters in integrated-circuit-compatible micro scale technologies have led to a maturing field resulting in dozens of MEMS bandpass filters in many different processes.

An electromechanical filter consists of a device which transduces input electrical energy into mechanical energy, filters it, and transforms the mechanical energy back into an electrical output. The transducers in the case of the filters designed here are variable capacitors, discussed in section 2.2. A collection of structures, which resonate with a very high quality factor, are coupled together to create a mechanical bandpass filter.

2.1 Using mechanical resonance to filter

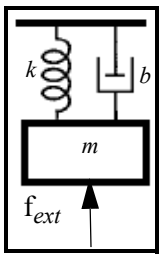

Figure 2-1. A mass spring damper system

The most basic mechanical filter is a simple mass, a linear spring and a damper such as the one shown in Figure [2-1]. An external force, the input, sets the mass in motion. When the mass pulls the spring from its resting position it transfers energy into the deformed spring. In this process, it loses some energy to the environment, with the dashpot drawn in the model symbolizing the source of this damping. At some point the reaction force of the spring overcomes the inertial force of the mass, and the mass swings back in the other direction. If the input force happens to pull back at just the point the mass would begin to swing back anyway — that is, if the input force is at the natural frequency of the mechanical system — the mass will resonate, as long as the system is underdamped. Equation [2-1] shows all the forces acting on the mass, where m is the mass of the resonator, **x** its displacement, a its acceleration, k the

spring constant of the attached spring (considering only linear springs for the moment), v the mass's velocity, b its damping factor, and f_{ext} the external force which excites it.

$$f_{ext} = ma + kx + bv = m\ddot{x} + b\dot{x} + kx \tag{2-1}$$

Considering the same simple system in the frequency domain, the next equation is the transfer function for the system.

$$\frac{X(s)}{F(s)} = \frac{1}{s^2 m + sb + k} = \frac{1}{m(s - s_1)(s - s_2)} = \frac{1}{k\left(1 + \left(\frac{s}{\omega_r}\right)^2 + \frac{s}{Q\omega_r}\right)}, \tag{2-2}$$

where the poles are $s_{1,2} = -\frac{b}{2m} \pm \sqrt{\left(\frac{b}{2m}\right)^2 - \frac{k}{m}}$, the natural frequency ω_r is $\sqrt{\frac{k}{m}}$ and the quality factor Q is $\frac{\sqrt{mk}}{b}$.

Systems that are useful for bandpass filters must be highly underdamped, minimizing b compared to k and m. Figure [2-2] shows the frequency response in a narrow band around resonance of such a system. It compares various values of damping, starting with an overdamped system and decreasing to a much smaller value which allows for a very large resonant peak: the shape desired for a narrow bandpass filter. With this very small damping compared to k and m, the poles s1,2 described above are actually very close to $\pm j\sqrt{\frac{k}{m}}$, the natural resonant frequency of the mass and spring.

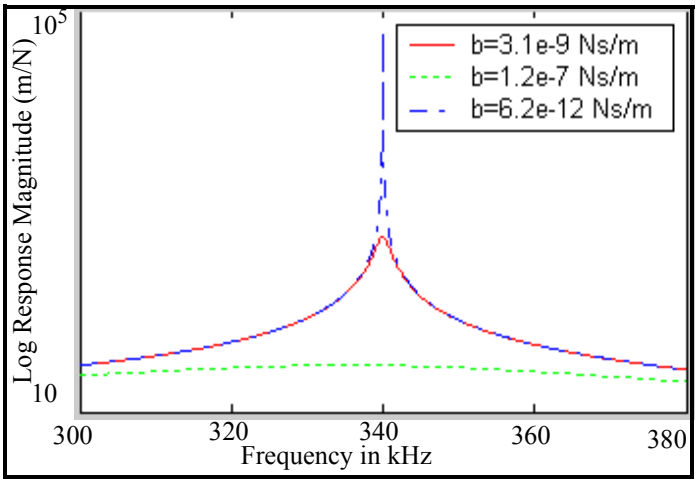

Figure 2-2. Frequency response of a cantilever resonator, whose displacement vs. force can be described by Equation 2-2. The values shown are for a mass m=.26 ng and spring constant k=1.19 N/m. The solid line shows the anticipated squeeze film air damping for the resonator, which will be discussed in later sections.

The ideal bandpass filter response sought in this work has a flat passband with a ripple of less than 10%. To achieve a flatter, wider shape, multiple poles must spread the passband over a wider frequency range. To add more poles, we must add more mass-spring subsystems.

One way to achieve a filter shape with the desired polynomial ratio is to construct one block of resonators for each pole-zero pair in the function [7]. The output of the first block is the only input into the second block, which feeds the next, and so on. The final function is the product of all the block transfer functions. The resonant frequencies of the blocks are deliberately slightly different, since each accounts for one conjugate-pair pole of the final polynomial. With tuning to ensure that

process variations don't move the poles too far from their intended positions, this can be a very simple approach. It eases the difficulty of coupling resonators, and the output of each stage can be electrically amplified before being passed on to the next stage, potentially greatly improving the filter's total conversion loss. With such a system, the challenge would be to be able to achieve specific resonant frequencies with great accuracy. In practice, because achieving highly specific resonant frequencies is very difficult, generally a better way to implement the desired transfer function is to add more individual resonators (mass-spring-damper combinations) and couple them together with additional springs, as in Figure [2-3]. Now the force is applied to the first mass and the output is the displacement of the final mass.

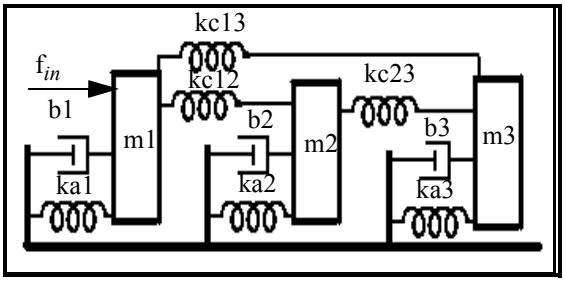

Figure 2-3. A system of three masses and dampers with springs connecting all the masses

Repeating the process above, equations [2-3] - [2-4] develop the transfer function for a system of multiple masses from the sum of forces on each mass *i* in a system of *n* masses and *n* dampers. Each mass may be connected by up to *n* springs: each mass can be connected to any of the other *n*-1 masses or to an anchor. Spring k_{ij} connects mass *i* to mass *j*, numbering from 1 to *n* for masses. An index of 0 indicates that the spring is anchored. Note that the anchoring springs and coupling springs are subscripted a and c in Figure 2-3 and Figure 2-4.

$$f_{exti} = m_i a_i + \left(\sum_{j \neq i}^{n} k_{ij}(x_i - x_j) \right) + b_i v_i = m_i \ddot{x}_i + b_i \dot{x}_i + \sum_{j \neq i}^{n} k_{ij}(x_i - x_j) \tag{2-3}$$

A Laplace transform of these sums-of-forces equations yields:

$$F_i(s) = X_i(s) \left(s^2 m_i + s b_i + \sum_{j = 0, j \neq i}^{n} k_{ij} \right) - \sum_{j = 0, j \neq i}^{n} k_{ij} X_j(s) \tag{2-4}$$

using upper-case letters to denote frequency-domain variables. Solving this linear system for the output, $X_n(s)/F_1(s)$ gives a filter with *n* conjugate-pair poles and up to *n* zeros.

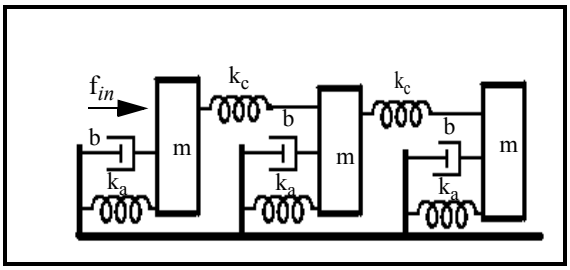

Figure 2-4. Three mechanical subsystems composed of 3 identical mass/anchor spring pairs coupled to the adjacent subsystem by springs of coupling constant kc.

The process of placing the poles and zeros of a bandpass filter is well-established. In filters constructed from Chebyshev polynomials, the subcircuits are symmetric: the resonators must be added in identical pairs (except for a single center resonator when the number of resonators is odd), with identical coupling environments [7]. For the identical resonator subcircuits, the resonator masses should be identical, each anchored on one side to a fixed point ($k_{i0} = k_a$) and also to its input and output neighbor as shown in the three-resonator system of Figure 2-4. There will be *n* conjugate-pair poles for the *n* resonators. The first pole will be at the natural frequency of the individual resonators. The spacing to each of the next poles is determined by the coupling springs. This method is well suited to fabrication tolerances in CMOS MEMS: although it's extremely difficult to achieve narrow absolute tolerances on device dimensions, very good matching can be done between devices [8]. It's also possible to make an array of slightly more filter blocks than are needed so that the absolute process variations, which determine the absolute filter center frequency, can be accounted for by using some of the "extra" filters, which have been drawn to be slightly too high in frequency or slightly too low, so that after the process variations they are just what is needed.

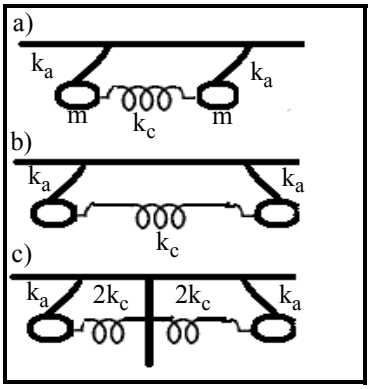

Figure 2-5. a) System of two masses coupled by a coupling spring, at resonance with resonant subsystems in phase. b) Same system with resonant subsystems 180 degrees out of phase. c) Equivalent subsystem for antiphase mode of b).

A commonly cited diagram, reproduced in Figure 2-5 for a system with two identical mass-spring resonators coupled by a third coupling spring, can give some insight into the physical principles underlying the positions of the poles in a system with identical resonators and coupling springs [7]. When both subsystems of mass *m* and spring k_a vibrate at their individual resonant frequencies, in phase, (part b) of the diagram) the coupling spring is neither stretched nor compressed, no energy is stored or released from it, and it can be ignored in calculating the resonant frequency, f_1, of this mode, which is simply $\sqrt{\frac{k_a}{m}}$.However, when the masses vibrate in anti-phase, they pull or push the spring in opposite directions, so that the center of the spring is not displaced at all, but the total stretching of the coupling spring is twice the displacement for each side. This means that the single coupling spring can be modeled as two springs of twice the stiffness (because each is now half the length), each attached to one of the masses on one side and anchored on the other as shown in part

c). This yields a net spring constant for each subsystem of $k_a + 2k_c$, as shown in d) for a resonant frequency f_2 of $\sqrt{\frac{k_a + 2k_c}{m}}$.

This argument can be extended to a system of *n* subsystems: for *n* resonator subsystems with *n-1* coupling springs, there are *n* relevant phase combinations which result in *n* different equivalent coupling spring values and *n* poles. A similar diagram Figure 2-6 shows the three important phase combinations for a system of three resonators [7].

To construct a two- or three-resonator filter, then, we first choose the center frequency, bandwidth and number of resonators. (Eventually the desired ripple will specify the number of resonators, but for this early work, we limit the maximum number of resonators to be cascaded in a single system to three.) Next, we determine the frequencies of the poles. In the case of a two-resonator system, the relation of the second frequency to the first is set by a single variable, the coupling spring constant, so a Chebyshev polynomial is possible. In an advanced system, the bandwidth and maximum ripple can both be determined independently, but in this early research, because we are limiting the number of cascaded resonators to two or three, either the bandwidth must be narrower than the desired 10 kHz, or the quality factor of the resonators must be brought down, or the maximum ripple limit must be sacrificed. We experiment with the second two options, as the quality factor can be dynamically lowered during operation, as will be described later. The relation between quality factor and ripple is illustrated in Figure 2-7.

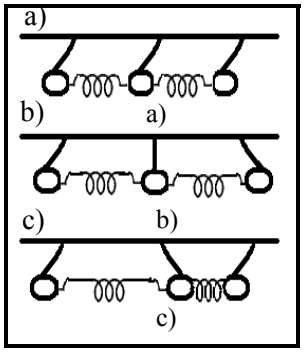

Figure 2-6. System of three identical resonators coupled by two identical coupling springs. a) Mode where all three are in phase b) 180 degree phase shift between outer and inner, with center motionless. c) 180 degree phase shift between each pair of neighbors.

Table 2-1 shows the transfer functions, pole locations and resonant frequencies for the simple mechanical system described here for two and three resonator systems.

The next step of MEMS filter creation is to design the resonator itself, which should have an anchor spring constant to effective mass ratio that gives it the resonance frequency needed for the first pole of the transfer function. The ratio of the coupling spring constant to the resonator anchor spring constant at the point of coupling determines the relative location of the next pole. Using the resonance frequency calculations from Table 2-1 and the resonator anchor spring constant, we find the coupling spring constant needed to set the second resonance frequency at the second pole of the transfer function. We design a coupling spring with this spring constant and couple the resonators with this spring.

Of course, the spring-mass-damper model of the physical system can give only an estimate of system performance. In reality the structure can deform in an infinite number of ways, which would have to be modeled with an infinite number of different "springs" and "masses," each with its own mode and frequency response, with the final shape of the deformed structure a superposition of all the shapes for the different spring and mass combinations. Even when the structure deforms primarily in the desired shape, the linear spring model only holds to a certain point: past that point, the internal strain creates a significant third-order nonlinear mechanical response. A similar effect in the transduction mechanism will also be encountered in the next section.

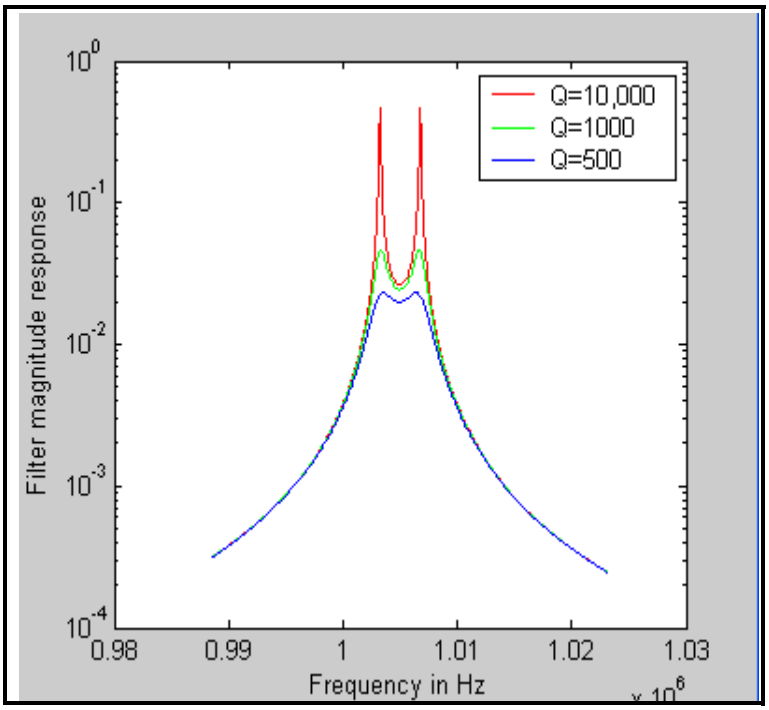

Figure 2-7. Comparison of ripple in a two-resonator, 10 kHz-wide bandpass filter with 1.05 MHz center frequency for three resonator quality factors

Another difficulty is that any physical coupling spring will also have mass. In macroscopic mechanical filters the size of the coupling spring can be much, much less than the size of the resonator, but at the very small scale of MEMS filters, the sizes are of about the same order, so

the mass of the coupling spring must play a part in the design of the system [9].

Table 2-1. Cascaded mechanical system transfer functions and poles for two and three-resonator systems

Number of resonators	Transfer function	Conjugate pole locations, s, s*	Ignoring damping, ω_1	Relative locations of higher poles
2	$\frac{k_c}{(s-p1)(s-p2)(s-p3)(s-p4)}$	$-\frac{b}{2m}\pm\sqrt{\frac{b^2}{4m^2}-\frac{k_a}{m}}$ $-\frac{b}{2m}\pm\left(\sqrt{\frac{b^2}{4m^2}-\frac{k_a+2k_c}{m}}\right)$	$\sqrt{\left(\frac{k_a}{m}\right)}$ $\sqrt{\left(\frac{k_a+2k_c}{m}\right)}$	$\omega_2 = \omega_1\sqrt{1+\frac{2k_c}{k_a}}$
3	$\frac{k_c{}^2}{(s-p1)(s-p2)\ldots(s-p6)}$	$-\frac{b}{2m}\pm\sqrt{\frac{b^2}{4m^2}-\frac{k_a}{m}}$ $-\frac{b}{2m}\pm\left(\sqrt{\frac{b^2}{4m^2}-\frac{k_a+k_c}{m}}\right)$ $-\frac{b}{2m}\pm\left(\sqrt{\frac{b^2}{4m^2}-\frac{k_a+3k_c}{m}}\right)$	$\sqrt{\left(\frac{k_a}{m}\right)}$ $\sqrt{\left(\frac{k_a+k_c}{m}\right)}$ $\sqrt{\left(\frac{k_a+3k_c}{m}\right)}$	$\omega_2 = \omega_1\sqrt{1+\frac{k_c}{k_a}}$ $\omega_3 = \omega_1\sqrt{1+\frac{3k_cc}{k_a}}$

2.2 Electrostatic actuation and mixing

All of the devices fabricated in this research are electrostatically actuated and sensed. A fixed electrode to one side of a resonator interacts with an electrode on the resonator itself, spaced a short distance away, forming a capacitor. The simple electromechanical resonator shown in Figure 2-8 illustrates the principle. The electrical energy contained in this configuration is simply the energy contained in the capacitor formed by the two electrodes: $\frac{1}{2}CV^2$, where C is the capacitance of the electrode combination and V is the voltage across the gap. The force between the fixed and resonator electrodes is then the derivative of this energy with respect to the gap, $\frac{d}{dg}\left(\frac{1}{2}CV^2\right)$, where *g* is the gap spacing. For parallel plates in which the dimensions of the electrode plates are much greater than the gap spacing, C can be estimated to be $\frac{\varepsilon hl}{g}$, for a force pulling the electrode and beam together of approximately $\frac{V^2\varepsilon hl}{2g^2}$, where ε is the dielectric constant of the material between the electrodes, *h* is the thickness of the electrodes, and *l* is their length.

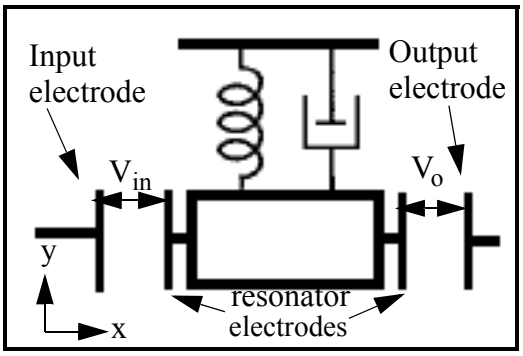

Figure 2-8. A voltage applied between the input electrode and the mass's left electrode (V_{in}) creates a force pulling the mass towards the input electrode. When the mass moves towards or away from the output electrode, the change in capacitance between the mass's right electrode and the output creates a small output current.

Because the resonator moves under the applied force, the magnitude of the force itself changes with the motion: $g(t) = g_0 + x(t)$, where g_0 is the initial gap and $x(t)$ is the displacement of the resonator input electrode. (For linear comb finger drives, the motion of the fingers is parallel to the gap, so the force remains constant. Comb finger drives are difficult to work with at the scale needed for the frequencies of interest for this research, so all the structures discussed here move perpendicularly to the gap, making the gap spacing a function of time. Future research could address linear electrostatic drives at these frequencies.) This displacement-dependence of the magnitude of the force at the input electrode looks like:

$$_{in}(t)= \frac{-v_{in}(t)^2 \varepsilon h l}{2g(t)^2} = -\frac{v_{in}(t)^2 \varepsilon h l}{2(g_0 + x(t))^2} \approx \left(-\frac{v_{in}(t)^2 \varepsilon h l}{2{g_0}^2}\right)\left(1 - \frac{2x(t)}{g_0} + \frac{3x(t)^2}{g_0^2} + \ldots + \frac{(-1)^n n x(t)^{n-1}}{g_0^{n-1}}\right), \quad (2\text{-}5)$$

taking n terms of a Taylor series approximation for the final equation. Repeating the same process in Equation 2-6 for the force exerted on the resonator by the output electrode shows that although the first term of the Taylor series approximation describes the force pulling the mass towards the electrode, the even, displacement-dependent terms always pull the mass in the direction of the displacement: these terms act as "negative" springs.

$$f_{right}(t)= \frac{v_o(t)^2 \varepsilon h l}{2g(t)^2} = \frac{v_o(t)^2 \varepsilon h l}{2(g_0 - x(t))^2} \approx \left(\frac{v_o(t)^2 \varepsilon h l}{2{g_0}^2}\right)\left(1 + \frac{2x(t)}{g_0} + \ldots + \frac{n x(t)^{n-1}}{g_0^{n-1}}\right) \quad (2\text{-}6)$$

This effect is called spring softening: the resisting spring force seen by the mass under the electrostatic load is the sum of the mechanical spring force and the negative electrostatic spring force, making the system spring constant appear smaller and the spring softer. If the voltage is very large, this spring softening can have a noticeable effect on the resonance frequency of the resonator. In fact, it can be used to tune the resonance frequency to make up for processing variations. The second term of the Taylor series expansion of Figure 2-6 is the linear electrostatic spring constant, $k_e = \frac{-V^2 \varepsilon h l}{g_0^3}$. The new resonance frequency, including the effects of the electrostatic spring forces on the input and output electrodes, is

$$f_r = \frac{1}{2\pi}\sqrt{\frac{k_m + k_{e,in} + k_{e,out}}{m}} = f_m \sqrt{1 + \frac{k_{e,out} + k_{e,in}}{k_m}}, \quad (2\text{-}7)$$

where k_m is the mechanical spring constant and f_m is the resonance frequency without any electrostatic force applied. (Here, upper-case variables denote frequency-domain functions, whereas lower case variables are in the time domain. This leaves the subscript to differentiate between force and frequency variables.)

The higher order terms of this approximation are also relevant in filter design, particularly for avoiding distortion in the passband, discussed in section 2.2.2.

2.2.1 Sensing

An additional fixed electrode on the other side of the beam can be used to detect the motion of the beam electrically when a DC "polarizing" voltage exists between the resonator and the fixed output electrode: as the beam moves towards and away from the output electrode, the changing electric field generates a small displacement current. Modeling this again in terms of the changing capacitance between a resonator electrode and the output electrode, the output current is

$$\frac{dQ}{dt} = \frac{d}{dt}(CV) = V\frac{dC}{dt} = \frac{V\varepsilon hl}{(g_0 - x(t))^2}\frac{dx}{dt}, \tag{2-8}$$

assuming V to be constant.

This output signal magnitude is linearly dependent on the voltage across the capacitor. This DC polarizing voltage may be one of the easiest parameters to control to raise the filter's output signal magnitude. The maximum practical DC voltage, V_p, is set by intermodulation distortion limits, discussed below, and by the maximum DC pull-in voltage. The DC pull-in voltage is the voltage at which the DC force is high enough to snap the resonator mass to one of the fixed electrodes. Because the electrostatic force increases nonlinearly as the gap closes but the resisting spring force is linear, at a displacement of 1/3 of the gap for an ideal parallel plate capacitor the electrostatic spring force pulling in becomes stronger than the spring force pulling back. The DC voltage across any of the gaps, therefore, must be kept small enough that the DC displacement of the mass is less than 1/3 of the gap; however, in a symmetric arrangement in which the V_p is applied to both sides of the mass and the fixed electrode DC voltages are the same, the DC forces pulling the mass toward the fixed electrodes cancel each other and as long as they are much less than the mechanical spring restoring force the resonator will not veer to either side. In this configuration the maximum DC voltage is limited by the mechanical spring constant. In practice, distortion considerations contribute more to the practical limit on sensitivity and output magnitude.

As mentioned previously, the filter output comes from a current created at the output electrode due to the motion of the resonator. Equation 2-8 assumed a static voltage on both electrodes of the output capacitor. In fact, the voltage at the output may vary, affecting both the output signal and the motion of the resonator itself. A more inclusive discussion of the output signal comes in section 2.3.

2.2.2 Mixing and force components at various frequencies

Since the force on the beam is dependent on the square of the voltage, the device can be used as a mixer. Table 2-2 shows some of the combinations of input voltages that are used in this project, the components of the force at various frequencies these inputs create, and the relative magnitudes of these force components.

Table 2-2. Components of force at various frequencies for various configurations of voltages on input electrodes

Fixed Input Electrode Voltage	Voltage on Resonator's Moving Input Electrode	Frequencies and Relative Sizes of Force Components
$V_{rf}\cos\omega_{rf}t$	$V_{lo}\cos\omega_{lo}t$	$2\omega_{rf}$.....$\frac{1}{2}V_{rf}^2$ $2\omega_{lo}$.....$\frac{1}{2}V_{lo}^2$ $\omega_{rf}+\omega_{lo}$.....$-V_{rf}V_{lo}$ $\omega_{rf}-\omega_{lo}$ .....$-V_{rf}V_{lo}$ 0 (DC).....$\frac{1}{2}V_{rf}^2+\frac{1}{2}V_{lo}^2$
$V_{rf}\cos\omega_{rf}t$	V_p	$2\omega_{rf}$.....$\frac{1}{2}V_{rf}^2$ ω_{rf}.....$-2V_{rf}V_p$ 0 (DC).....$\frac{1}{2}V_{rf}^2+V_p^2$
$V_{rf}\cos\omega_{rf}t$	$V_{lo}\cos\omega_{lo}t+V_p$	$2\omega_{rf}$.....$\frac{1}{2}V_{rf}^2$ $2\omega_{lo}$.....$\frac{1}{2}V_{lo}^2$ $\omega_{rf}+\omega_{lo}$.....$-V_{rf}V_{lo}$ $\omega_{rf}-\omega_{lo}$ .....$-V_{rf}V_{lo}$ ω_{rf}.....$-2V_{rf}V_p$ ω_{lo}..... $2V_{lo}V_p$ 0 (DC).....$\frac{1}{2}V_{rf}^2+\frac{1}{2}V_{lo}^2+V_p^2$

Most MEMS resonators to date have used the fundamental frequency as the input frequency, using the input combination of row 2 of Table 2-2. Using a high polarizing voltage on the resonator eases the selection of the fundamental over the other modes, as generally the DC voltages

in the system can be much larger than the AC magnitudes. Some MEMS filters use DC voltages as high as 250 V and many are above 100 V, whereas the AC voltages tend to range from mV in vacuum to up to 10 V in air [8]. In addition to the perhaps 100-fold larger force component at the fundamental frequency achievable by putting a polarizing voltage on the resonator across from the input fixed electrode, the mechanical structure itself has a high stopband rejection, so the force components at other frequencies are generally filtered out.

For downconverting mixer-filters, in which the force component desired is at the lower difference frequency between the two AC inputs, ω_{rf}-$\omega_{lo,}$ using a high DC polarizing voltage doesn't help increase the input force: the force component of interest depends only on the magnitude of the two AC inputs. Since the high-frequency mixer-filter input magnitudes in a practical communications system will be limited by dynamic range and linearity of the transistors of the previous stage, they will generally be small. Optimizing the mechanical system for a high selectivity is therefore essential. If a polarizing DC voltage is present at the resonator input as in row 3 of Table 2-2, the unwanted force component at the RF and LO frequencies may be much larger than the force components at the desired difference frequency: in this case in particular, the stopband rejection must be high. Generally, it's preferable to avoid this problem by separating the polarizing voltage needed for sensing the motion at the output from the AC voltages needed to excite the motion by sending two wires down the resonator.

Although the magnitude of the driving forces in a downconverting mixer-filter may have a much lower maximum value than the driving forces in a filter driven directly at its fundamental frequency, this limit may be offset by the advantage of not having any large input signal at the frequency of the output. Feedthrough through unavoidable parasitic capacitances threatens to swamp the filtered signal when large amplitudes at the signal frequency are used to drive the resonator into motion; in a mixed system the only components at the difference frequency are due to noise and interferers.

2.2.3 Distortion due to non-linearity in the force

Returning to Equation 2-5 on page 13, we can see how the various components of force due to the squared time-varying voltage term and due to the higher-order time-varying displacement-dependent terms can interact to introduce intermodulation distortion (IMD). A very strong interferer *anywhere* in the frequency spectrum can cause an inappropriate response at the resonance frequency. Consider, for example, the effects of the fourth term in the Taylor series approximation for the electrostatic force, $-4\frac{V(t)^2 \varepsilon h l}{2g_0^5}x(t)^3$. A powerful interferer, even at a frequency deep in the

mechanical stopband, will cause small vibrations at the interferer's frequency: $x_1 = \alpha \sin(\omega_1 t)$. A small amount of noise at the frequency $\omega_2 = 2\omega_1 - \omega_r$ will interact with the vibration at ω_1 in this Taylor series $x(t)^3$ term, where x(t) is now $\alpha \sin(\omega_1 t) + \beta \sin(\omega_2 t)$. The third power of this sum contains a component at the frequency ($2\omega_1 - \omega_2 = \omega_r$), creating a force component at the resonance frequency. Because the resonator's damping is so low, even a very small spurious force at the resonance frequency will cause a large response [11].

Note that this particular Taylor series term is not the only contributor to intermodulation distortion in the force, nor are these frequency relationships the only ones which result in spurious components at the resonance frequency: interactions of voltage components at various frequencies, which are squared, with any of the time varying displacement terms will also produce IMD, as will higher order displacement terms. The mechanical spring equation also has terms at higher powers of the displacement, although the magnitude of these terms is much smaller than the magnitude of the electrostatic terms.

Predicting the actual value of the intermodulation distortion is tricky, not only because there are a large number of terms, but because for larger displacements the parallel plate simplification of the capacitance breaks down: the resonator electrode displacement is not the same across the entire electrode, nor is the gap uniform. Also, for the higher-order displacement-dependent terms, the dependence on the initial gap size is of such a high order that small deviations in fabrication due to processing variations will strongly affect the magnitude of the non-linearity. For the initial designs fabricated for this thesis, the intermodulation distortion has not be explicitly predicted. During testing, a value of the polarizing voltage and the maximum displacement which result in an acceptable intermodulation distortion limit is sought.

2.3 Sensing and output circuitry

The output circuitry for MEMS mixer-filters is as much a part of the device as the mechanical structure. The previous calculations for the transduction of motion to and from electronic signals assumed that the voltage across the output capacitor was constant. In fact, it may vary considerably, and any voltage that appears on the MEMS "output" electrode creates a force across the "output" gap, feeding back to the resonator and adding to or opposing its motion. The input characteristics of the output circuit therefore play a role in determining the resonant frequency of the device and its quality factor.

Imaginary components of the circuitry impedance seen at the MEMS output electrode affect the mechanical vibration by sloshing energy back into the system, either in or out of phase

with the resonator velocity. Because of their phase response relative to the velocity of the resonator, inductive components of this impedance contribute to the mass term in the sum of forces equation for the mass. Capacitive components contribute to the spring term. The impedance will also probably have some real components, which will dissipate some of the resonator energy: resistive components contribute to the damping term in the sum of forces equation. The effects of the circuitry impedance are addressed in more detail in the next section.

Similarly, parasitic feedthrough capacitances from the inputs to the output store and reinject energy into the system and affect its frequency response.

2.3.1 What's needed from the output circuit

An ideal output circuit provides a convenient, known DC potential for the output electrode, without degrading the signal or introducing noise or damping into the resonator. It amplifies the output enough to make it easily used by other circuits. It provides an output impedance appropriate to the successive electronics. It introduces no electronic noise. This ideal amplifier creates no harmonics, faithfully reproducing the frequency spectrum of the resonator, or, even better, passing the resonator passband and further rejecting its stopband. The perfect circuit also picks up no stray signals from sources other than the MEMS resonator output. Differential amplification and common mode rejection are also needed for the differential topologies fabricated here. The common mode rejection is essential for diminishing interfering feedthrough, power supply variations, common-mode noise, and ground bounce.

Perhaps the most awkward requirement for the on-chip output circuit is that of providing the known DC bias for the output electrode. Figure 2-9 shows some of the biasing schemes commonly used or proposed for MEMS resonators. A resistive connection to a known voltage adds noise to the electrode. Worse, the output signal current from the mixer-filter generates a voltage at the vibrating frequency on the output electrode. This voltage, which is proportional to the velocity of the resonator, creates a feedback force that damps the resonator's motion. In the sum-of-forces equation for the resonator system, such as Equation 2-3, this voltage contributes a new term to the velocity-dependent damping term, increasing the total damping and decreasing the Q of the system.

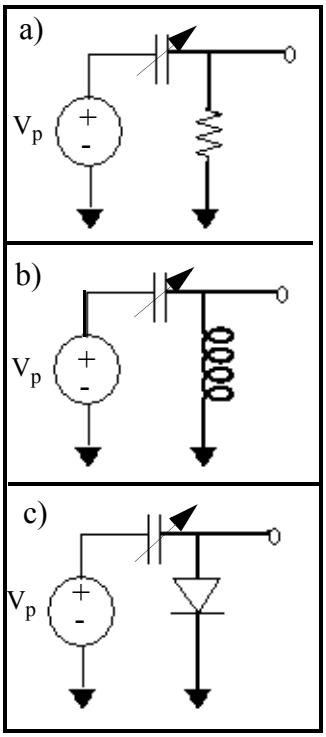

Figure 2-9. Electrical equivalents for DC biasing schemes for the resonator output electrode. In each case, the output can be read as a voltage at the marked node or as a current emerging from the "grounded" side of the load impedance. a) Using a resistive path to a known voltage (shown here as dc ground). b) An inductive biasing impedance. c) A bias impedance whose resistance varies with the voltage across it. Diodes have been used in the past, but other devices, such as the subthreshold transistors used for this research, are also possible.

An inductive connection from the output electrode to a known potential also creates an AC voltage on the output, opposing the MEMS output current. Again, this AC voltage creates additional components of force on the resonator. Interesting functions can be created, but the inductor size and the complexity make this an unappealing approach for initial research.

The third DC biasing element is an active circuit which biases the output electrode voltage whenever it exceeds a certain threshold voltage, as with the diode shown. An alternative is a small transistor biased below its threshold by tieing its gate and source to the same known potential. The latter has been used in CMOS MEMS inertial sensors [12]. Ideally, this approach takes the best features of each biasing type: at DC, the impedance is resistive, providing a DC bias for the output electrode through the large resistance of the subthreshold transistors. But the load at the higher frequencies of the mixer-filter passband is essentially capacitive, arising from the input capacitance of the amplifier and the parasitic capacitances of the MEMS device itself. Avoiding a resistive load at the operating frequencies decreases the damping in the system and improves the Q.

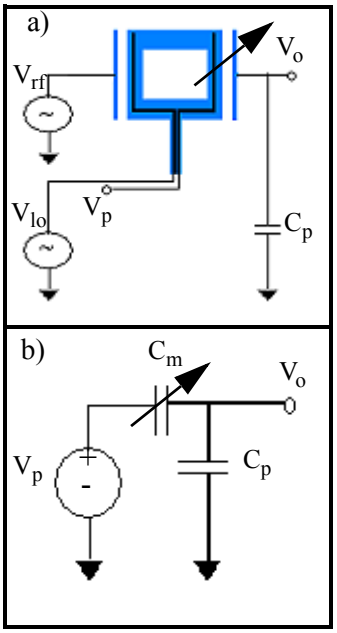

Figure 2-10. a) MEMS resonator, with input electrodes configured for mixing, and output capacitive load. b) Small signal circuit equivalent linearized around the operating point for MEMS device and subthreshold transistor-biased differential voltage amplifier.

Returning to the issue of the effects of the impedance on the resonator, we see that the changing electric field from the resonator's motion creates an AC voltage at the output node. This voltage creates another component of force on the resonator, affecting its vibration. We start with the output current $i_{out}(t) = \frac{d}{dt}[C_m(t)(V_p - v_o(t))]$ going through the MEMS sense capacitor. Setting the currents through the MEMS and parasitic capacitors equal, we get

$$(V_p - v_o(t))\frac{\varepsilon h l}{(g_0 - x(t))^2}\frac{d}{dt}x(t) - \frac{d}{dt}v_o(t)\left(\frac{\varepsilon h l}{(g_0 - x(t))} + C_p\right) = 0 . \qquad (2\text{-}9)$$

This equation is simplified by replacing the variable capacitance terms with the first two terms of their Taylor series approximation. We eliminate all the terms at frequencies other than the primary vibration frequency, assuming that the stopband rejection makes the contributions at other frequencies small enough to ignore:

$$\frac{V_p C_s}{g_0} sX - sV_o C_s - sV_o C_p = 0, \tag{2-10}$$

where $C_s = \frac{\varepsilon hl}{g_0}$. Equation 2-11 finds the force on the resonator due to the voltage on the output electrode.

$$f_{out} = \frac{1}{2}(V_p - v_o(t))^2 \frac{d}{dx} C_m(t) = \frac{1}{2}(V_p - v_o(t))^2 \frac{\varepsilon hl}{(g_0 - x(t))^2} \tag{2-11}$$

Again returning to a Taylor series approximation, the component of this force at the vibration frequency is $\frac{-C_s V_p v_o(t)}{g_0}$. Adding this force to the input-electrode force to get the sum of forces equation for the resonator yields

$$m\ddot{x}(t) + k\dot{x}(t) + bx(t) = f_{in} - \frac{C_s V_p v_o(t)}{g_0}. \tag{2-12}$$

Solving these two equations in the two unknowns x(t) and $v_0(t)$ in the frequency domain leads to new transfer functions for the displacement and output voltage,

$$\frac{X(s)}{F_{in}(s)} = \frac{1}{ms^2 + bs + k + \frac{C_s^2 V_p^2}{(C_s + C_p) g_0^2}} \tag{2-13}$$

$$\frac{V_o(s)}{F_{in}(s)} = \frac{C_s V_p}{(C_s + C_p) g_0 \left(ms^2 + bs + k + \frac{C_s^2 V_p^2}{(C_s + C_p) g_0^2} \right)}. \tag{2-14}$$

The poles are now:

$$s_{1,2} = -\frac{b}{2m} \pm \sqrt{\left(\frac{b}{2m}\right)^2 - \frac{k}{m} - \frac{C_s^2 V_p^2}{g_0^2 m (C_s + C_p)}} \tag{2-15}$$

showing a spring-stiffening term k_{cap} of $\frac{C_s^2 V_p^2}{g_0^2 (C_s + C_p)}$ due to the parasitic capacitance. For larger, stiffer resonators, larger capacitive loads, higher Q, and larger gaps, the output force effect due to the capacitance diminishes.

For comparison, the previously-discussed spring *softening* term is $k_e = \frac{-V^2 C_s}{g_0^2}$. Note that the signs for k_{cap} and k_e are different because the force components arise from very different phys-

ical mechanisms. The spring softening arises from the nonlinear electrostatic force, as discussed in section 2.2. In contrast, as the resonator approaches the output plate, the output voltage grows, decreasing the electrostatic force pulling the resonator in. This force works *with* the mechanical spring, restoring the mass to its undeflected position.

Figure 2-11 shows the results of a simulation comparing the output of a MEMS cantilever resonator with different capacitive loads, illustrating this spring hardening effect. To demonstrate the capacitive loading effect, the polarizing voltage V_p is held constant so the electrostatic spring softening doesn't change.

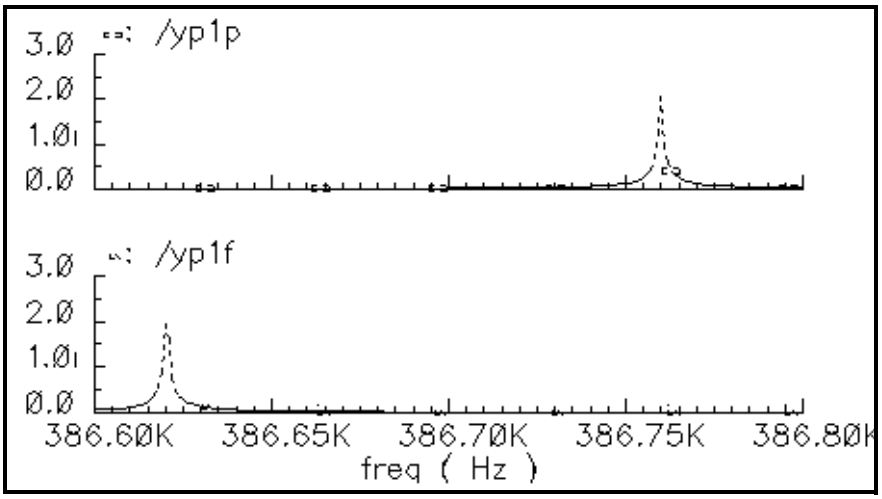

Figure 2-11. A Cadence simulation using Nodas models [13] of a cantilever resonator, showing normalized displacement near the resonance frequency of the cantilever. In a) the output electrode has a 1 pF capacitor connecting it to ground. In b) the output electrode is connected to ground through a 1 fF capacitor. Note that the large capacitor raises the resonant frequency about .4%, matching hand calculations of the frequency shift. The output magnitude and Q also rise slightly for the larger load, as predicted.

One last thing to note about a purely capacitive load is that it does not introduce any loss into the critically sensitive stage of the filter, and so does not diminish the Q at all. In fact, a slight improvement in the Q accompanies the slight rise it causes in the spring constant and resonant frequency.

2.4 System transfer function and output

We develop a model of a complete subsystem driven at the difference frequency of RF and LO signals on the input electrodes, including the input and output transduction. The force, calculated in Equation 2-6 for resonators driven as in row 1 of Table 2-2, has useful components only at the lower difference frequency of the input voltages. To solve for the transfer function for displacement as a function of the RF input voltage magnitude, $\frac{X(s)}{V_{rf}(s)}$, we must also solve for the voltage on the output electrode, as in the previous section. The sum of forces equation is:

$$m\frac{d^2}{dt^2}x(t) + b\frac{d}{dt}x(t) + kx(t) = -\frac{1}{2}(v_{rf}(t) - v_{lo}(t))^2\frac{\varepsilon h_{ed} l_{ed}}{(g_{0d} + x(t))^2} + \frac{1}{2}(V_p - v_o(t))^2\frac{\varepsilon h_{es} l_{es}}{(g_{0s} - x(t))^2} \qquad (2\text{-}16)$$

where the subscript *ed* and *es* denote the drive and sense electrodes respectively. Replacing the capacitance equations with the first one or two terms of the Taylor series approximation, as appropriate to keep all the terms at the primary vibration frequency, and then performing a Laplace transform on Equation 2-16 gives:

$$\left(ms^2 + bs + k - \frac{V_p^2 C_s}{g_{0s}^2}\right)X(s) + \left(\frac{V_p C_s}{g_{0s}}\right)V_o(s) = \frac{v_{rf} v_{lo} C_d}{g_{0d}}, \tag{2-17}$$

where C_d and C_s are the nominal capacitances of the drive and sense nodes. Then, using Equation 2-9 for the output electrode voltage V_o and solving the linear system, gives

$$X(s) = \frac{v_{rf} v_{lo} C_d}{g_{0d}\left(ms^2 + bs + k - \dfrac{C_p C_s V_p^2}{(C_s + C_p) g_{0s}^2}\right)}. \tag{2-18}$$

The output voltage V_o is

$$V_o(s) = \frac{V_p v_{rf} v_{lo} C_s C_d}{g_{0s} g_{0d} (C_s + C_p)\left(ms^2 + bs + k - \dfrac{C_p C_s V_p^2}{(C_s + C_p) g_{0s}^2}\right)} \tag{2-19}$$

The poles of both equations are

$$s_{1,2} = -\frac{b}{2m} \pm \sqrt{\left(\frac{b}{2m}\right)^2 - \frac{k}{m} + \frac{C_s C_p V_p^2}{g_{0s}^2 m (C_s + C_p)}} \tag{2-20}$$

The last term, again, is the combination of the spring hardening from the output capacitance and the spring softening from the polarizing voltage.

The MEMS voltage "gain" at resonance, then, is:

$$\frac{V_o(j\omega_r)}{V_{rf}(j\omega_r)} = \frac{-jV_p v_{lo} C_s C_d}{\omega_r g_{0d} g_{0s} b (C_s + C_p)} = \frac{-jV_p v_{lo} \varepsilon^2 h_{ed} h_{es} l_{ed} l_{es}}{\omega_r g_{0d}^2 g_{0s}^2 b (C_s + C_p)} \tag{2-21}$$

and the Q is:

$$Q = \frac{\sqrt{m\left(k - \dfrac{C_p C_s V_p^2}{g_{0s}^2 (C_s + C_p)}\right)}}{b}. \tag{2-22}$$

2.4.1 Coupling mechanisms

Looking at the components of the transfer function for one complete electromechanical subsystem, we can see several points at which one subsystem can couple to the next. Several coupling mechanisms are enumerated below.

1. The subsystems can be coupled with physical springs, as described already and shown in Figure 2-4 part a).
2. They can be coupled electronically by transducing the mass displacement to an electrical signal which is then transduced back into the force on the next subsystem, as shown in part a) of Figure 2-12.
3. They can be coupled electronically as in 2) but with amplification of the electrical signal before it is applied to the next subsystem, as shown in part b) of Figure 2-12.
4. They can be coupled with an electromechanical spring, as shown in part c) of Figure 2-12.

A shared electrode between the output side of one resonator and the input side of the next implements coupling method 2 [14],[15]. The idea is that the output signal current of the first subsystem draws charge to or from one side of the small shared electrode, altering a voltage on the other side of the shared electrode. This voltage change drives the second subsystem just as the RF and LO signals drive the first. The size of the shared capacitance is critical: the smaller the capacitance, the larger the coupling signal. Applying a known DC bias to the shared electrode can be a challenge: because the signal current is tiny, any off-chip connections add degrading capacitance and active connections add noise and capacitance. At the cost of delay (phase change), simply amplifying the current output into a larger voltage input for the next stage, probably with an amplifier which will at the same time give the output node a known DC bias, is a good alternative with potentially negligible insertion loss.

The fourth coupling method uses the electrostatic forces between the output electrode of one resonator and the input electrode of a resonator placed nearby. Equation 2-23 adapts the force calculation in Equation 2-5 for two variables to obtain the force on the input electrode of the second of a cascaded pair of resonators: now both electrodes can move. This assumes that the output side of the first resonator is grounded and the input side of the second is charged to a voltage V_{spr}. x_1 and x_2 are the displacements of the first and second subsystems' electrodes.

$$f_{21}(t)= \frac{-V^2 \varepsilon hl}{2g(t)^2} \approx \frac{-V_{spr}{}^2 C_0}{2g_0}\left(1 + \frac{2x_1(t) - 2x_2(t)}{g_0} + \frac{3x_2^2(t) - 3x_1^2(t) - 3x_1(t)x_2(t)}{g_0^2} + \ldots\right) \tag{2-23}$$

Using only the terms directly proportional to the displacement, the coupling spring constant k_e is $\frac{-V_{spr}{}^2 \varepsilon hl}{g_0^3}$. Note that this spring constant is negative, unlike mechanical spring constants, so the poles due to modes in which resonator subsystems vibrate out of phase are *lower* than the resonators' natural resonance frequencies.

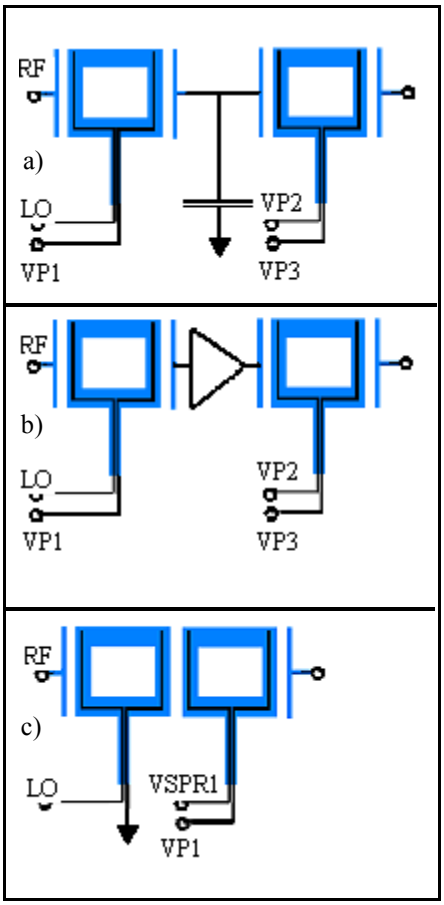

Figure 2-12. Electrical coupling methods. Method 2 in part a), method 3 in part b), and method 4 in part c).

2.4.2 Sensing the right thing

Because the output signal in a MEMS mixer-filter can be extremely small, currents at unwanted frequencies may often be larger. In an ideal chip, there would be no capacitance between the RF input and the output. Likewise, the only capacitance between the LO and the output on a resonator configured as in row 3 of Table 2-2 would be the output electrode capacitance, which in the resonators of this research is in the range of about .1 fF. In this case, the only feedthrough current would be $i_{i_{lo,\,fdthrough}} = -v_{lo}\omega_{lo}C_0\sin(\omega_{lo}t)$, where we assume that the nominal output and input MEMS capacitances are both C_0. Even at very high LO frequencies, the ratio of the feedthrough current to the signal current,

$$\frac{|i_{lo,\,fdthough}|}{|i_s|} = \frac{v_{lo}\omega_{lo}C_0}{\left(\frac{V_p v_{lo} Q C_0^2}{2kg_0^2}\right)} = \frac{\omega_{lo}2kg_0^2}{V_p Q C_0} \qquad (2\text{-}24)$$

given a high quality factor, is still very reasonable. However, in practice, particularly in our test systems in which wirebond pads link LO and RF to many internal nodes without intervening circuits, a few fF of capacitance from pads, wirebonds and cables may develop between LO, RF and the output. The output current is so tiny that even this small parasitic—which is most likely larger than the resonator electrode capacitance—creates a relatively large current, especially when LO and RF are high frequency signals. If this feedthrough is not carefully handled, it may swamp the signal current.

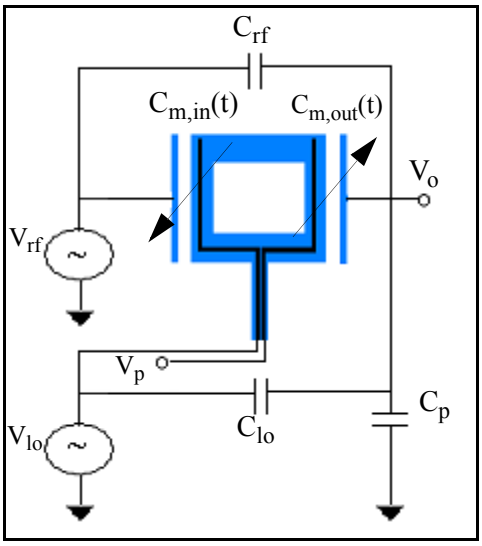

Figure 2-13. Capacitors in a single resonator.

Clearly, layout must take the utmost care to minimize these parasitics, but even so, some current will feed through. One solution is to feed the current into a pream-plifier with a very large dynamic input range and a frequency roll-off not much higher than the resonance frequency, which will reject these larger but higher frequency components. Another approach, the one taken here, is to replicate the resonator, feed both versions with the same RF and LO but opposite Vp, so that the feedthrough is significant and in phase, and feed the output into a differential pre-amplifier with a very large common mode rejection ratio and input dynamic range.

3 Topology analysis

The first step of developing a MEMS mixer-filter is selecting a mechanical resonator topology. This chapter follows the process of selecting and optimizing the actual CMOS MEMS springs and masses to implement the resonators described in Chapter 2.

The spring mass system selected should fulfill the following general criteria:

1. It should have a single primary mode of resonance which is dominant over all other modes.
2. It must have adequate electrical output magnitude: the minimum acceptable output current targeted in this research is 10 nA into ground.
3. At that level of sensitivity, it must introduce intermodulation distortion at a level of -20 dB or less.
4. Its resonance frequency must be fairly insensitive to fabrication variations or it must have a dynamic tuning mechanism which allows its resonance frequency to be pulled to the planned frequency after processing inaccuracies move it.
5. It must be cascade-able.
6. It must be amenable to a mechanical or electrical arrangement that rejects unwanted capacitive feedthrough from the inputs.
7. It should have low damping.

To take advantage of the nearly trivial electronics integration possible with CMOS, we wish to fabricate the mixer-filters in CMOS MEMS. The CMOS MEMS technology which presents a few unique challenges earlier MEMS resonators have not had to contend with. The most important are listed below.

1. CMOS MEMS released structures are composed of CMOS metal interconnect blocks and the insulators below them. The choice of cross sections is limited in CMOS MEMS: the available heights are the distances from the substrate to the top surfaces of the metal interconnect layers. In each case the top layer must be metal and the lower metal layers may be included or omitted as needed. Some of the stack is oxide, a less-than-desirable material for an electrode. The limited maximum stack height is a concern in designing lateral resonators, in which the thickness of the electrodes greatly influences the sensitivity of the device. In comparison, lateral resonators used in some other mixer-filters have 15 to 80 μm-thick silicon electrodes [4],[14],[15].

2. In CMOS MEMS the silicon substrate cannot be separately contacted: any wells put under a CMOS MEMS resonator are simply etched away. The surface underlying CMOS MEMS structures will always be at the lowest CMOS potential on the chip. The much-publicized MEMS resonators that use a vertically resonant clamped-clamped beam in which the width of the electrode can be arbitrarily large [16],[17] are not possible in CMOS MEMS.
3. Residual stress between and within layers may be relatively large and is determined by the foundry. Stress relief mechanisms must be designed into every structure long enough to be critically affected by compressive stress. Cantilevers and other sufficiently compliant structures may curl vertically.
4. The minimum gap achievable between any two electrodes without post-assembly is determined by the CMOS foundry's minimum line spacing. This limits the smallest gaps to about .5 μm, much larger than the 65 to 300 nm gaps reported for gaps created from sacrificial oxide layers [14],[18],[16],[19].
5. Because the composite structure is often composed of multiple metal layers, mask misalignment may deform the device.

Besides the integration with CMOS circuitry, which has enormous benefits for the readout of the very small signals from MEMS resonator-based filters, using CMOS as the foundation for resonator design allows us to use the multiple interconnect layers within the moving resonator structure in very useful ways not available in processes that use single conducting layers for their released devices.

3.1 Topology selection

To achieve a high resonance frequency, $\sqrt{\frac{k}{m}}$, the spring constant k must be large and the mass m must be small. The limits on the size of the mass tend to eliminate linear comb-drive based designs, both because their mass complicates achieving a high resonance frequency and because at the very small dimensions required for high frequencies, the bulk required for the comb fingers introduces unwanted modes that begin to interfere with the desired mode. In fact, simplicity becomes a major goal of the design in order to avoid unwanted modes.

One of the simplest possible structures is a beam. A beam must be attached to the substrate somehow to anchor it. Successful MEMS resonators have demonstrated the advantages of a variety of different anchor points: some beams are anchored on one end and free on the other, anchored on both ends, or attached at a node somewhere along the length.

Fixed-fixed beams -- clamped at both ends --are especially desirable because they have higher spring constants for the same mass than other configurations. However, fixed-fixed beams are sensitive to residual stress: tension in the beam raises the resonant frequency of the structure and decreases its sensitivity, and compressive stress reduces the resonant frequency and increases the sensitivity. Too much compressive stress buckles the beam and disastrously cripples its response.

CMOS MEMS structures suffer from some residual stress within and between the thin layers of metal and oxide, which varies over temperature. The residual stress problem may be solved by anchoring the fixed-fixed structure to a released plate suspended from the wafer by crableg springs or other stress-relieving supports, but this is a topic for further research.

To avoid problems with unknown or variable compressive residual stress, the majority of devices in this initial research are cantilevers, whose unclamped ends are free to expand, relieving the axial compressive stress. Node-clamped "free-free" beams, which have the advantage of greatly reduced internal damping losses to the supports [16], are a good subject for future research: the topologies from previous research using vertical free-free beam resonators are impractical in CMOS MEMS because of the layer stack and the inability to control electrodes below the structure.

In addition to targeting specific resonance frequencies, it is desirable to maximize the selectivity (Q) and output current magnitude of the devices. In general terms, the quality factor of a single resonator device is $\frac{\sqrt{mk}}{b}$. Holding the resonance frequency fixed at the desired $\omega_r = \sqrt{\frac{k}{m}}$, the quality factor is $\frac{m\omega_r}{b}$, so larger, stiffer resonators have higher quality factors if the damping remains the same. Operating under conditions in which squeeze film damping dominates all other damping sources, for the same size squeeze plates and gap, larger resonators have better selectivity.

Adapting Equation 2-21 on page 22 for the case of symmetric input and output electrodes, the maximum output signal amplitude is:

$$\frac{V_o(j\omega_r)}{V_{rf}(j\omega_r)} = \frac{-jV_p v_{lo} C_s C_d}{\omega_r g_{0d} g_{0s} b(C_s + C_p)} \approx \frac{-jV_p v_{lo}(\varepsilon h_e l_e)^2}{\omega_r g_0^4 b C_p}, \qquad \textbf{(3-1)}$$

where the final approximation assumes that the parasitic capacitance, C_p, is much larger than C_s. However, Equation 3-1 is misleading in indicating that the output magnitude can arbitrarily be increased by increasing the drive signal strength, because it omits two essential features of the electrostatically driven system: the danger of exciting the mechanical vibration to such an amplitude that it crashes into the fixed electrodes, and the dependence of the filter function's linearity on the maximum amplitude. Combining Equation 2-18 and Equation 2-19 on page 22, it can be seen that if the amplitude of the system is restricted to a certain proportion of the total gap, say αg_0 then v_o at resonance becomes instead:

$$v_o(t) = \frac{V_p C_s x(t)}{g_{0s}(C_s + C_p)} = \frac{V_p C_s \alpha g_{0s} \cos(\omega_r t)}{g_{0s}(C_s + C_p)} \approx \frac{V_p C_s \alpha \cos(\omega_r t)}{C_p} = \frac{V_p \varepsilon h_e l_e \alpha \cos(\omega_r t)}{g_{0s} C_p} \qquad \textbf{(3-2)}$$

Assuming that the system mechanical Q is high enough that the driving forces can be set to whatever levels are necessary to achieve a vibration amplitude of αg_0, we then re-examine the output

current magnitude using Equation 3-2. To maximize the output magnitude, the dc polarizing voltage, V_p should be as large as possible. The maximum polarizing voltage that can be used without snapping the resonator to one of the electrodes is also determined by the stiffness, as can be seen in Table 3-1. Thus, stiffer resonators gain sensitivity, assuming circuit limitations do not force V_p far below the pull-in voltage. Note that although previous equations considering the input force dependence show that the output magnitude depends on the square of the MEMS static capacitance and the fourth power of the gap, removing the dependence on the input force and keeping the physical limits of the gap in mind brings those dependences down to linear dependence on the MEMS capacitance and the gap.

Squeeze-film air damping at the micron to slightly sub-micron scales fabricated for this research can be approximated as having a damping factor, [20]

$$b = \frac{96\mu_a l_e h_e^3}{\pi^4 g_0^3}, \qquad \textbf{(3-3)}$$

where μ_a is the viscosity of air around the device. This assumes the plates of the electrodes are flat, the gap is uniform, and the operating frequency is well below the cutoff frequency, $\omega_c = \frac{P_0 \pi^2 g_0^2}{12\mu_a h_e^2}$, calculated at ambient pressure to be 165 MHz. This damping contribution to the system Q indicates the opposite directions in scaling dimensions to maximize the output signal magnitude as the previous discussions for the mass and spring constant. Smaller plates have lower damping, and this dependence goes as the cube of the electrode thickness. The gap dependence is also reversed: larger gaps yield lower damping and increase Q, and the damping is related to the cube of the gap distance. Equation 3-4 calculates the maximum output voltage for a squeeze-film-damped resonator with symmetric input and output electrodes.

$$\frac{V_o(j\omega_r)}{Vrf(j\omega_r)} = \frac{-jV_p v_{lo}(\varepsilon h_e l_e)^2}{\omega_r g_0^4 b(C_s + C_p)} = \frac{-j\pi^4 \varepsilon^2 V_p v_{lo} l_e}{192\mu_a g_0 \omega_r (C_s + C_p) h_e} \qquad \textbf{(3-4)}$$

The surprising result is that the output magnitude is now only linearly proportional to the electrode length, and *inversely* proportional to its thickness, assuming that the parasitic capacitance dwarfs the MEMS variable capacitance.

However, these devices are intended to be operated in vacuum, where air damping will be brought down to a level below or near other damping sources. For this initial work, in determining sizing of the resonators, the damping sources are treated as constant for all geometries, and the other parameters are manipulated to achieve larger output magnitude. Future research will explore quan-

tifying the other sources of damping in CMOS MEMS resonators and finding optimal sizing guidelines for deep vacuum operation.

3.2 Cantilever resonators

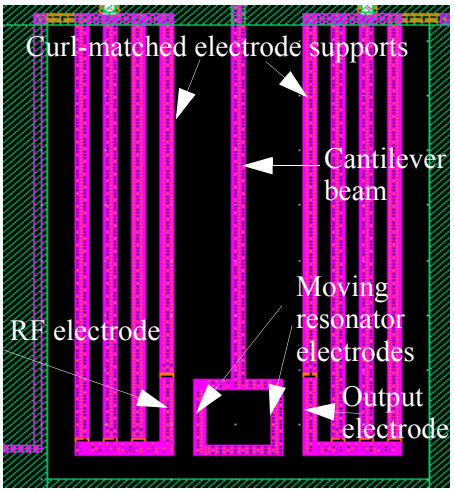

Figure 3-1. Cadence layout of a 400 kHz cantilever fabricated in the TSMC .35 μm process.

Although cantilever resonators are smaller than clamped-clamped resonators of the same frequency for the same electrode thickness and beam width, making them more sensitive to process variations, they are robust to variations in compressive residual stress in the CMOS stack. For the frequencies of interest here, they can also be made short enough that residual-stress-gradient induced vertical curl is either not significant, or easily matched by released equal-length truss-stiffened electrodes with the same residual stress gradient.

The cantilever resonator examined most closely in this work, shown in Figure 3-1, features a wide electrode on the end of the cantilever beam. In general, most single-beam resonators place electrodes along a small section of the beam to achieve better linearity and to make modeling simpler. The wide spacing of the electrode plates of the square on the end of the cantilever is intended to cut down on parasitic capacitance between the inputs and the output, at the cost of somewhat more mass and complexity, and significantly transduction electrode area. Another benefit of this electrode head is that it leaves large open areas around the cantilever beam, easing the problem of etching the narrow electrode gaps.

Figure 3-2. Model of the 400 kHz cantilever. The outline shows the undeflected position and dimensions. The shaded form is the shape at resonance under a uniform y-directed distributed load on the left electrode plate, with the shading indicating the relative displacement.

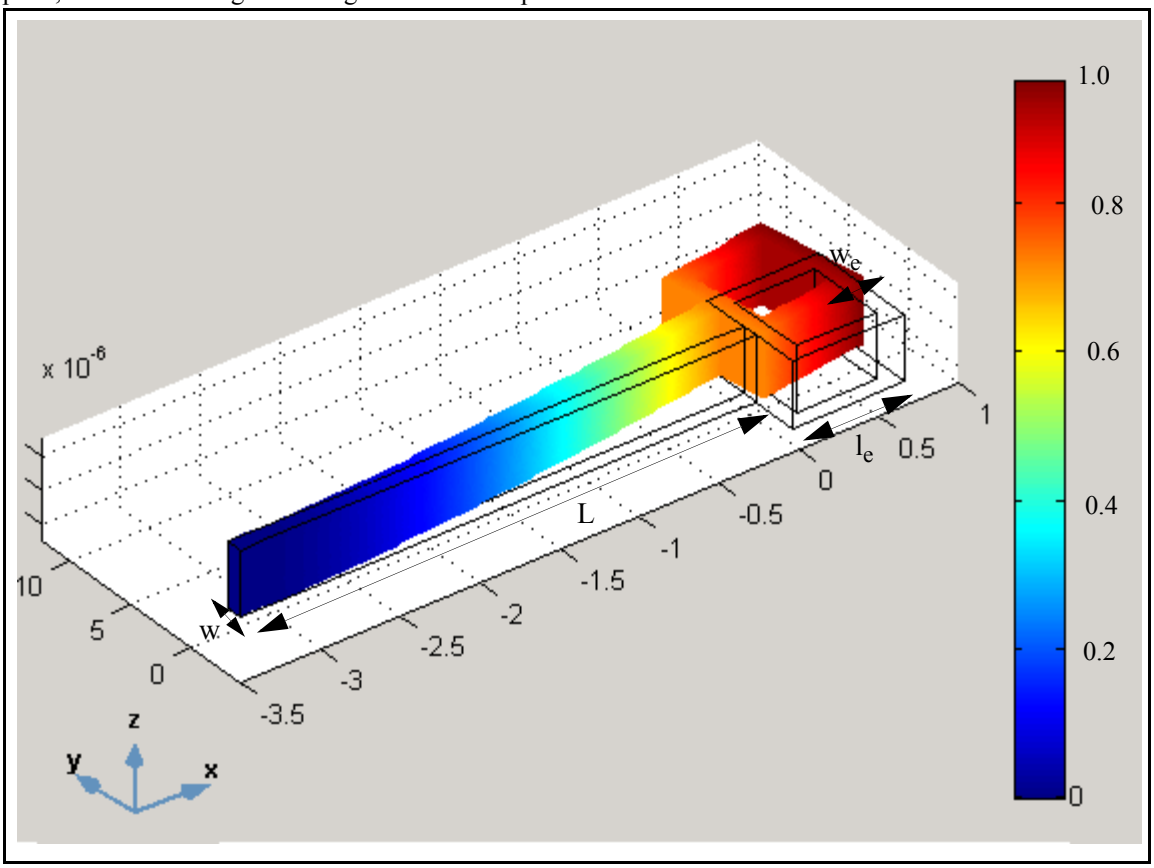

To model the cantilever's mechanical response, every element of the resonator is reduced to a component or force at the center of the electrode, and the cantilever beam itself is modeled as an Euler beam. The electrode on the tip is very helpful in simplifying the modeling: the electrode itself is modeled as a point mass at the centroid of the cantilever electrode and the distributed electrostatic load along the electrode is modeled as a point force at the same point. Points on the structure's mass are weighted by their contributions to the entire structure's kinetic energy, so that the structure's mass can also be modeled as a point mass at the electrode centroid. Finally, the electrode head is modeled as a rigid body that deflects in a line along the angle of the tip of the cantilever.

Table 3-1 shows the hand calculations used to model this type of cantilever. This assumes that the width is less than the thickness so that the primary mode of resonance is lateral, not vertical. It also assumes that the electrode length and mass are less than the cantilever beam length and mass: at long electrode lengths, the electrode begins to deform significantly relative to the cantilever beam, and the assumptions these equations are based on fail. Appendix 1 also contains the Matlab code to find the effective mass of this cantilever for a given set of dimensions.

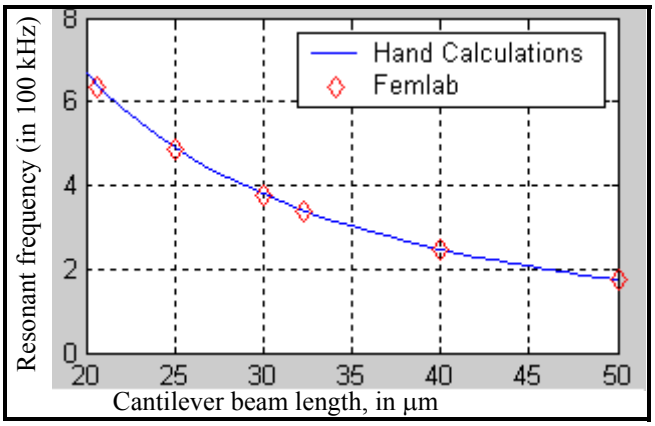

Figure 3-3. Comparison of resonant frequencies over a range of cantilever beam lengths for a cantilever with a 7-μm-long square electrode, as pictured in Figure 3-1. FEMLab simulations confirm the results of the hand calculations, even for the shortest cantilevers.

All the cantilever electrodes constructed in this research are 7 μm long, and the shortest beam length is 19 μm, well within the acceptable length ratio of cantilever to electrode. Figure 3-3 compares the hand-calculated resonant frequencies for devices of various cantilever lengths to the resonant frequencies from a FEMLab simulation.

An additional topology consideration for these CMOS MEMS structures is mask misalignment. In the CMOS process used to fabricate these resonators, the thickest possible stack is composed of four different metal layers, so mask misalignments such as shown in Figure 3-4, are a significant concern. A misalignment of a metal layer mask in the resonator may raise the resonance frequency by increasing the beam width and therefore the spring constant. Such a misalignment would also decrease the gap size, perhaps even to the point that processing could not release the beam. For a beam with the cross-section shown in Figure 3-4 part b), where one side of the beam contains significantly more oxide along the outer edge than the other side, residual stress at the operating temperature may curve the electrode laterally, distorting the capacitive parallel plate arrangement. For these reasons, single-metal-layer beams, which self-align, are also attractive and a small number of these were fabricated. However, the much-lower transduction efficiency is a serious drawback, and most of the fabricated cantilevers are thicker.

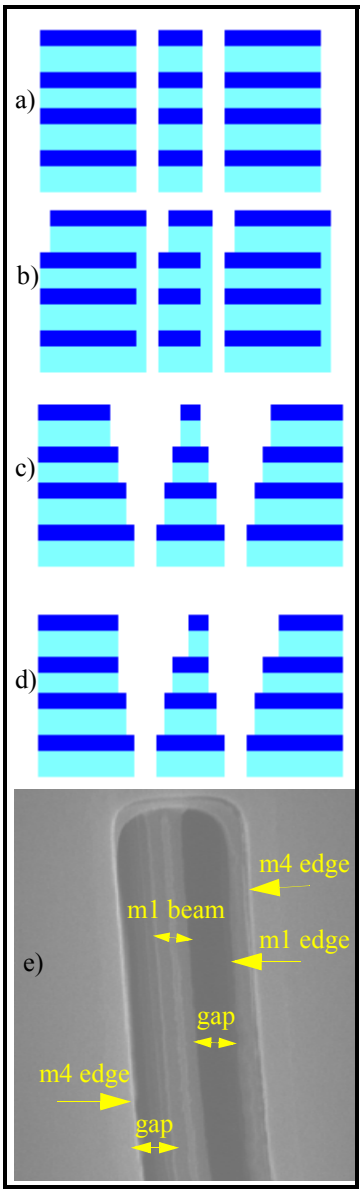

Figure 3-4. .Cross sections of CMOS metal (darker bars) and insulator layers (light bars) a) The stack with no mask misalignment b) The stack of figure a) with a metal 4 misalignment c) Insetting each layer of metal slightly from the next layer below. d) The effect of a metal 4 mask misalignment on c). e) An SEM of a metal 1 beam surrounded by metal 4. Misalignment of metal 4 -- it has shifted right relative to the lower layer, as in b)-- has distorted the position of the top electrode and possibly narrowed the gap on the left.

Another way to decrease the misalignment sensitivity is to pull the higher layers of metal in by slightly more than the maximum anticipated misalignment on each side [21]. The foundry used to create the devices for this research does not provide misalignment process variation information or guarantees, but the design rule for via layer overlap distance, which presumably ensures a generous probability that overlapping metal layers will continue to be connected after any likely misalignment, guided the decision to inset each successive metal layer by .2 μm from its lower neighbor. With this design, misalignments do not increase the beam width or affect the lower layers' gap width, and although there may still be some net residual stress due to the misalignment, the major asymmetry in oxide layers is eliminated so bending problems should be much less.

There are two somewhat separate sizing problems involved in designing these cantilever resonators: first, the dimensions of the electrode, which are largely responsible for the magnitude of the output signal, and second, of the cantilever beam, whose dimen-

sions are the primary determinants of the resonance frequency and Q of the structure. The next two sections describe the competing considerations for each

Table 3-1. Modeling equations for cantilever with a square electrode on the end. Here x is the distance along the x axis from the cantilever's anchor point, y is the cantilever beam's displacement along the y axis, L is its length, I is the cantilever beam's moment of inertia, w its width and h its thickness, as shown in Figure 3-2. The electrode length and width are l_e and w_e. E is the composite Young's modulus and r the composite density for the layers of oxide and aluminum.

Cantilever boundary conditions	1. The displacement at the anchor is 0. 2. The slope of the beam at the anchor is also 0. 3. The moment due to the electrostatic load f at the beam tip is $\frac{fl_e}{2}$. 4. The shear force due to the electrostatic load at the beam tip is -f.
Cantilever beam shape	$y(x) = \frac{f}{EI}\left(-\frac{x^3}{6} + \left(\frac{l_e}{4} + \frac{L}{2}\right)x^2\right) \Leftrightarrow y(L) = \frac{f}{EI}\left(\frac{L^3}{3} + \frac{L^2 l_e}{4}\right)$
Reference deflection (at center of electrode)	$y_{ref} = y\left(L + \frac{l_e}{2}\right) = y(L) + y'(L)\frac{l_e}{2} = \frac{f}{EI}\left(\frac{L^3}{3} + \frac{L^2 l_e}{2} + \frac{L l_e^2}{4}\right)$
Spring constant at center of electrode	$k = \frac{EI}{\frac{L^3}{3} + \frac{L^2 l_e}{2} + \frac{L l_e^2}{4}} = \frac{E w^3 h}{4L^3 + 6L^2 l_e + 3L l_e^2}$
Effective mass of cantilever beam	$m_{eff,beam} = \frac{m_{beam}}{L y_{ref}^2}\int_0^L y(x)^2 dx$
Effective mass of cantilever head	$m_{eff,head} = \frac{\rho l_e h}{y_{ref}^2}\int_L^{(L+w_e)} (y(L) + y'(L)(x-L))^2 dx +$ $\frac{2\rho w_e h}{y_{ref}^2}\int_{(L+w_e)}^{(L+l_e-w_e)} (y(L) + y'(L)(x-L))^2 dx +$ $\rho l_e h / y_{ref}^2 \int_{(L+l_e-w_e)}^{L+l_{ee}} (y(L) + y'(L)(x-L))^2 dx$
Natural resonant frequency	$f_r = \frac{1}{2\pi}\sqrt{\frac{k}{m_{eff,beam} + m_{eff,head}}}$
Damping in air, assuming two identical electrodes	$b = \frac{192\mu_a l_e h_e^3}{\pi^4 g_0^3}$
Q in air	$Q = \frac{\sqrt{km}}{b}$

Table 3-1. Modeling equations for cantilever with a square electrode on the end. Here x is the distance along the x axis from the cantilever's anchor point, y is the cantilever beam's displacement along the y axis, L is its length, I is the cantilever beam's moment of inertia, w its width and h its thickness, as shown in Figure 3-2. The electrode length and width are l_e and w_e. E is the composite Young's modulus and r the composite density for the layers of oxide and aluminum.

Electrostatic spring constant. $V_{dc,gap}$ is the dc voltage across the gap, including the circuit dc biases.	$k_e = \frac{V_{dc,gap}\varepsilon h l_e}{g_0^3}$
DC Pull-in voltage	$V_{pullin} = g_0^{\frac{3}{2}}\sqrt{\frac{8k}{27\varepsilon h l_e}}$
Electrode beam spring constant	$k_{electrd} = \frac{32 E w_e^3 h_e}{l_e^3}$

3.2.1 Cantilever electrode sizing

Equation 3-1 and Equation 3-2 show that to maximize the output current, the electrode overlap capacitance should be as large as possible: the resonator electrodes should be as long and thick as they can be made. However, the desire for a long electrode to increase transduction efficiency competes with the desire to keep the electrode small and stiff in comparison to the cantilever beam. We would like the cantilever beam to flex, setting the resonant qualities of the structure, while the electrode beams remain rigid. The last entry in Table 3-1 is the spring constant for the electrode beam of the electrode head, assuming a distributed load across the length of the electrode beam. We can use this as a sanity check, in addition to FEA analysis, to check that the electrode is much stiffer than the cantilever beam.

The cantilever length can increase proportionally to increase the electrode length without altering their mass ratios, but lengthening the electrode without also widening it makes it softer. To keep the electrode spring constant the same (it is roughly proportional to $\left(\frac{w_e}{l_e}\right)^3$) while doubling the electrode length would require twice the electrode width, a 4x increase in area. It is more space-efficient to double the *number* of resonators for the same increase in output current. The length of the electrode was arbitrarily set to 7 μm for all the cantilevers. In future research, if similar electrodes are used, the minimum electrode size should be set by the device with the highest operating frequency, as the output voltage magnitude is inversely proportional to the operating frequency with a capacitively loaded device.

Electrode width should be minimized to keep the mass of the electrode small relative to the cantilever beam mass. However, placing the RF input as far away as possible from the output elec-

trode cuts down on feedthrough. The four-beam electrode configuration shown in Figure 3-1 increases the distance between input and output electrode sides while keeping the mass low. A particular concern of this configuration is keeping the electrode beams as stiff as possible so that they bend as little as possible under the applied load, instead transmitting the force to the cantilever tip. For this reason the electrode width is always set larger than the minimum process width, to 1 or 2 μm.

It is extremely desirable to minimize the gaps for the best sensitivity. However, the limitations of MEMS release processing are not yet entirely clear, so drawn gaps varying from 1.5 μm down to the minimum allowed by the CMOS process design rules were fabricated. The smallest gaps have proven a challenge for postprocessing and so far have not been successfully released.

3.2.2 Cantilever beam sizing

The length and width of the cantilever beam are linked by the target resonance frequency. In sizing the cantilever beams for a given resonance frequency, the main advantages of larger beams are:

- The sensitivity to process variations diminishes. The average processing variations become a smaller proportional variation.
- Stiffer, larger resonators may also have higher Q, depending on the damping, as discussed in section 3.1.
- Stiffer, larger beams have higher pull-in voltages. The pull-in voltage rises as the square of the spring constant. In this case the pull-in voltage goes as a factor of $w^{3/2}$ so the output current magnitude can be increased by the same factor.
- Stiffer resonators are less sensitive to voltage noise, which affects the electrostatic spring softening, and therefore moves the resonant frequency of the device.

The disadvantages of larger beams are:

- Another drawback to stiffer, wider beams is that they require tuning voltages to be larger, since the tuning range is dependent on the ratio of the electrostatic tuning spring to the mechanical spring.
- As the length of a cantilever beam grows, so does the residual-stress-gradient-induced vertical deflection of the tip of the cantilever. The curl radius of a cantilever is a function of the thicknesses of its various layers and their stresses [20]; experience with the specific CMOS process used is necessary to predict the curl. Once the radius of curvature for each layer combination is determined, the maximum allowable length of a cantilever can be set.
- For area efficiency, smaller is better. It would be very useful to be able to array very large numbers of resonators on a single chip: the goal is to use the smallest area possible to achieve the required output magnitude, linearity and Q.

Ideally, the thickness of the cantilever should be much greater than the width to suppress modes in which the cantilever vibrates vertically rather than from side to side, but the maximum height possible in CMOS MEMS is fixed by the selection of the top metal layer. As with the electrode thickness, mask misalignments are again a consideration. In particular, any misalignments that cause the beam to bend laterally will move the electrode closer to one electrode than the other, distorting the performance, or in the worst case, rendering the cantilever entirely inoperable. For this reason, self-aligned single metal beams and maximum-thickness beams in which higher metal layers are inset, as discussed for the electrodes, are the best options. Full-width, maximum-thickness beams were also fabricated.

The cantilever width and length are the primary determinants of the device's resonance frequency. The width will be the smallest dimension so will contribute most to processing-dependent variations in the resonance frequency: small increases in the width will greatly increase the robustness of the designed frequency to fabrication. However, the width should be much less than the thickness, which is again is limited by the CMOS process, to limit spurious vibration modes. Also, the wider the cantilevers are, the longer they must be to achieve the desired resonance frequency, and very long cantilevers will curl both vertically and laterally. Widths of 1, 2 and 3 μm were fabricated.

3.2.3 Tuning

Because process variations will cause shifts in the resonance frequency of fabricated devices from the designed frequency, some post-fabrication tuning mechanism is essential. An ideal tuning mechanism changes the resonance frequency of the device without decreasing Q or output magnitude, using any power, introducing any distortion, or interfering with cascading additional resonators.

To the author's knowledge, all voltage-controlled tuning for non-comb-drive resonators in published MEMS research uses the electrostatic spring effect to lower the resonance frequency by raising a dc voltage to increase the force in the direction of vibration. An example of an electrode configuration providing this kind of tuning for a cantilever is shown in Figure 3-5 a). Note that the same tuning voltage is applied to both sides of the resonator, avoiding any net force that would pull the resonator to one side, but doubling the tuning effect.

Many existing MEMS resonators use the polarizing voltage on the resonator itself to tune the resonance frequency rather than adding separate electrodes; this affects the resonator's sensitivity and alters the distortion level. The cantilever resonators that were most thoroughly tested in this

research do not have separate tuning electrodes and do have this tuning effect. Their electrostatic tuning spring constant is calculated in Table 3-1.

One of the disadvantages of putting tuning electrodes along the resonator is that because the resonant vibration changes the gap between the tuning electrodes and the resonator, intermodulation distortion occurs through interaction between the voltage across the gap and the resonator's motion. The placement of the electrodes along the base of the cantilever, where the motion is least, minimizes this effect but does not eliminate it. Even more distortion occurs when the cantilever is so narrow that the LO cannot be run down the center where it would be isolated from the tuning electrodes.

Part b) of Figure 3-5 shows an alternative method for tuning a cantilever resonator. The tuning electrode sits above the cantilever electrode, with its length parallel to the vibration direction. The tuning now occurs by applying axial tensile stress to the resonator. Assuming that the electrode angle change during resonant vibration is very small, the tuning gap changes very little during vibration. The tuning electrode is longer than the resonator electrode so even at maximum displacement there is no significant change in capacitance across the tuning gap and therefore no significant AC force component: the tuning force is constant. Instead, the DC axial force exerted on the electrode is transmitted to the cantilever tip, where it creates tension along the length of the cantilever.

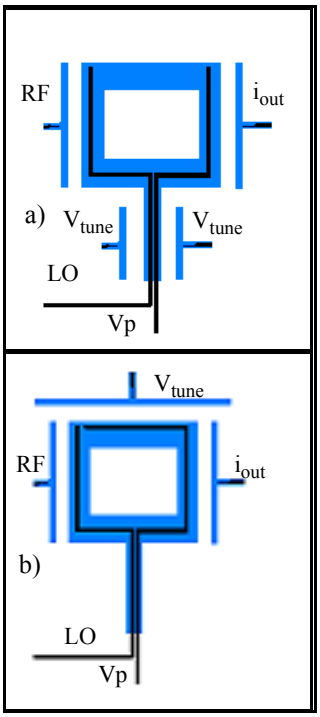

Figure 3-5. Electrostatic tuning mechanisms a) Traditional tuning force applied in direction of vibration. b) Tuning force applied perpendicular to vibration.

The axial force, F_t, on a 7-µm long, 3.52-µm thick electrode with a 1.5 µm gap is about .5 µN for a 100 V tuning voltage, which for a 1-µm wide, 32.3 µm-long cantilever in a 340 kHz resonator translates to a tuning spring constant

$$k_t = \frac{F_t}{l} \qquad \textbf{(3-5)}$$

of .015 N/m and a tuning range of about 2.5 kHz. Even better tuning ranges are possible, but errors in layout prevent testing of this principle with lower voltages and narrower (softer) cantilevers, and, concerned about misalignment and release, narrower gaps were not attempted. The tuning works much better for narrower, smaller, softer cantilevers as it is the ratio of the tuning spring constant to the mechanical spring constant that determines the tuning range. In any case, since the system will be tested in vacuum and the cantilever is very stiff in the direction of the tuning force, the limit

on the tuning voltage is very high. One last thing to notice is that the tuning voltage just discussed is the voltage across the tuning gap: the voltage applied to the tuning electrode is relative to the voltage on the resonator electrode, not ground. It may be a negative voltage rather than a positive one. Figure 3-6 shows a simulation of an axial-force tuning electrode.

Figure 3-6. Cadence AC analysis of the tuning effect for a Nodas model of a 7-µm long, 7-µm wide electrode with a 1.5 µm gap on a 32.3 µm long. 1 µm wide cantilever. The top graph shows the effect of the tuning on the output voltage, and the bottom shows the effect on the mechanical vibration amplitude. A 100-V potential has been placed across the tuning gap on the cantilever corresponding to vmemsma and ym1a (the right peaks), and 0V across cantilever corresponding to vmemspa and yp1a (the left peaks.) ym1a and yp1a are the displacement amplitudes of one of the outermost corners of the electrode square.

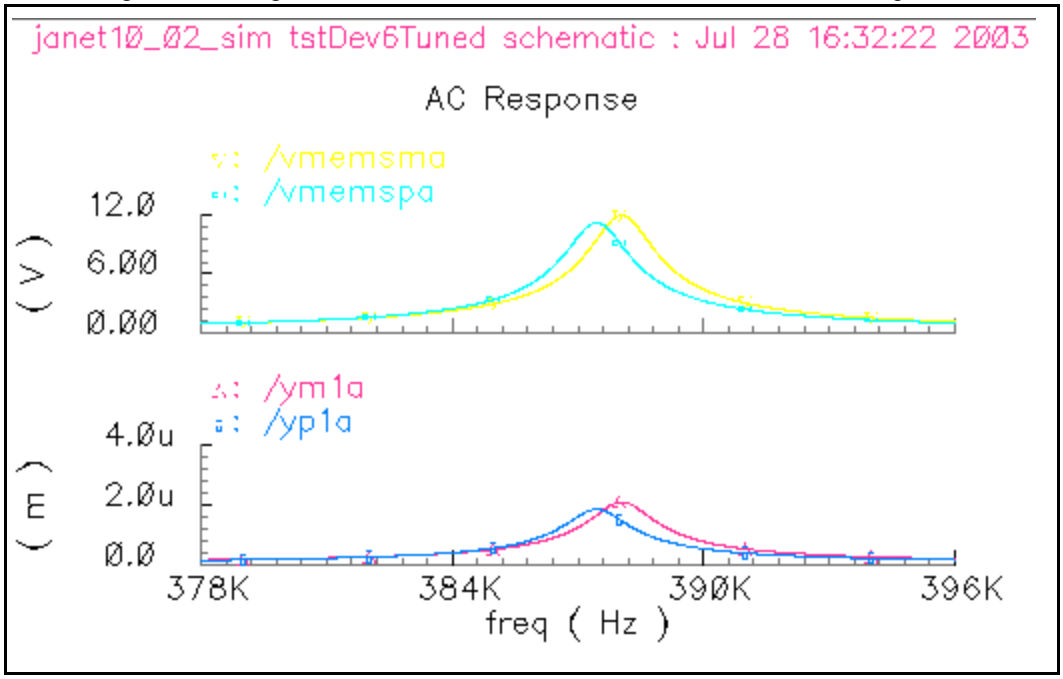

3.2.4 Wiring

Dealing with common-mode noise, power supply variations, substrate noise and the unwanted feedthrough and distortion currents outlined in section 2.2.2 and 2.4.2 calls for a replica of the entire device and differential sensing. The replica device is wired identically to the original except that the polarizing voltage is of the opposite sign. The *magnitude* of the difference of the fixed electrodes' DC potential and the polarizing voltage is the same. The mechanical vibration excited by the RF and LO difference frequency will be in phase in both devices but the signal output current will be of the opposite sign. Power supply noise, substrate noise, and feedthrough, however, will be the same in both devices (limited by local mismatch) and will appear as a common mode input to the differential amplifier to which the output connects. The differential amplifier also rejects the common-mode intermodulation distortion products due to interaction of the LO voltage with the mechanical vibration at the resonance frequency. It does not help the third-order intermod-

ulation distortion products which result from interactions between the polarizing voltage and other mechanical vibration components and voltage inputs; in fact, it doubles them because they appear 180 degrees out of phase at the two outputs.

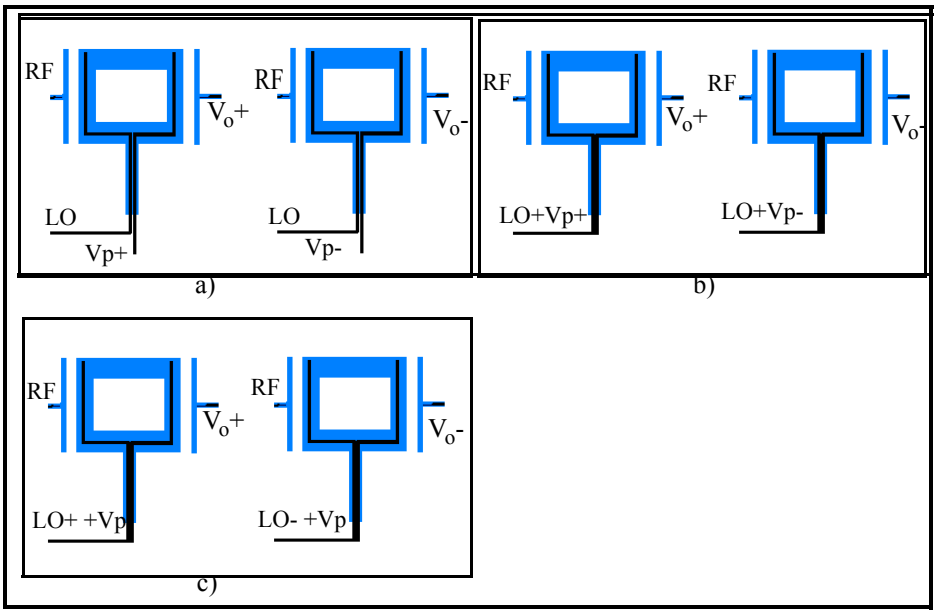

Figure 3-7. Wiring for cantilevers. In a) the LO and Vp are separate, the best arrangement. Mechanical resonance due to the RF/LO difference frequency is in phase but the output current is inverted in the second device. In b) the LO is added to the polarizing voltage, which is of the opposite sign in the two devices. The phase relations for the difference frequency-excited resonance are the same as in a). In c) the LO is again added to a polarizing voltage, but this time the Vp is the same in both cases and LO is inverted in the second device. The mechanical resonance is shifted 180 degrees in the second device, so the current is also.

Ideally the LO and the polarizing voltage are separated, cutting down dramatically on LO feedthrough and the interaction between V_p and the RF and LO voltages as well as additional mechanical modes. However, our initial resonators were fabricated with a single electrical wire presented on both input and output electrodes, as shown in Figure 3-7 b) and c). Figure 3-7 shows all the wiring arrangements fabricated for this project and Table 3-2 compares the magnitudes of their output current at unwanted frequencies. The second and third schemes limit the polarizing voltage

to a reasonable output voltage for a high-speed LO CMOS or BiCMOS driver, a severe limitation on the output magnitude and signal to noise ratio.

Table 3-2. Comparison of unwanted current components at the output node for the electrode wiring arrangements in Figure 3-7. In computing the distortion products it is assumed that noise is too small to have any significant effect, the mechanical stopband rejection is so high that force components at other frequencies are completely rejected, and that the output voltage v_s is so small compared to the other system voltages that its effects can be neglected. It is assumed that the input voltages generate an amplitude of vibration of αg_0. A final assumption, that the primary source of feedthrough capacitance is in the resonator itself, is the most suspect.

	Arrangement *a*	**Arrangement *b***	**Arrangement *c***
Input voltage 1	$V_{RF} + v_{rf}\cos(\omega_{rf}t)$ $-(V_{LO} + v_{lo}\cos(\omega_{lo}t))$	$V_{RF} + v_{rf}\cos(\omega_{rf}t)$ $-(V_{pp} + V_{LO} + v_{lo}\cos(\omega_{lo}t))$	$V_{RF} + v_{rf}\cos(\omega_{rf}t)$ $-(V_p + V_{LO} + v_{lo}\cos(\omega_{lo}t))$
Input voltage 2	$V_{RF} + v_{rf}\cos(\omega_{rf}t)$ $-(V_{LO} + v_{lo}\cos(\omega_{lo}t))$	$V_{RF} + v_{rf}\cos(\omega_{rf}t)$ $-(V_{pm} + V_{LO} + v_{lo}\cos(\omega_{lo}t))$	$V_{RF} + v_{rf}\cos(\omega_{rf}t)$ $-(V_p + V_{LO} - v_{lo}\cos(\omega_{lo}t))$
Mechanical phase	Same in both halves for difference frequency excitation	Same in both halves for difference frequency excitation	Opposite in the two halves
Output voltage 1	$V_{pp} - v_{s1}\cos(\omega_0 t)$	$V_{pp} + V_{LO} + v_{lo}\cos(\omega_{lo}t)$ $-v_{s1}\cos(\omega_0 t)$	$V_p + V_{LO} + v_{lo}\cos(\omega_{lo}t)$ $-v_{s1}\cos(\omega_0 t)$
Output voltage 2	$V_{pm} - v_{s2}\cos(\omega_0 t)$	$V_{pm} + V_{LO} + v_{lo}\cos(\omega_{lo}t)$ $-v_{s2}\cos(\omega_0 t)$	$V_p + V_{LO} + (-v_{lo})\cos(\omega_{lo}t)$ $-v_{s2}\cos(\omega_0 t)$
RF feedthrough	common-mode	common-mode	common mode
LO feedthrough	decreased by separation of LO and DC; common mode	common mode	magnified by differential sensing
Differential output electrode intermodulation distortion	$(V_p - V_s)C_0\alpha^2\omega_0\big\|_{2\omega_0}$	$(V_p - V_s)C_0\alpha^2\omega_0\big\|_{2\omega_0}$	$v_{lo}C_0\alpha\omega_0\big\|_{\omega lo + \omega 0}$ $v_{lo}C_0\alpha\omega_0\big\|_{\omega lo - \omega 0}$

3.3 Output circuitry

Practical minimum specifications for the amplification circuit for this research come from the test set-up used to characterize the MEMS mixer-filters. An ideal circuit would allow testing of the MEMS devices with no external processing of the signal required between the chip and the test equipment. In this setup, wirebonds connect the MEMS chip to a PCB board and then 50 Ω cables make the final link to 50-Ω-input-impedance network and spectrum analyzers. The output impedance of the on-chip amplification circuit should also be 50 Ω. The spectrum analyzer's noise floor is about -100 dBm, or about 2.2 μV, so assuming the MEMS device provides the targeted output current of 10 nA, the current to voltage gain, or transresistance, of the on-chip amplification circuit must exceed 220, preferably giving an amplification of at least a factor of 10 above the noise floor,

so exceeding 2,220. Clearly, the input-referred (to the MEMS output node) current noise should be considerably below 10 nA over the frequency range to be measured, preferably at least below 1 nA. The highest-frequency input signals to be tested for this initial research range up to 1-2 GHz, so to plan for the common mode rejection, we assume a worst-case "input-referred" feedthrough capacitance of 10 fF, yielding a common mode current of 126 μA per Volt of input signal. To bring the effect of the feedthrough at least a factor of 10 below the desired signal we need a common mode rejection of more than 10^5 for each Volt of required input magnitude. (Extremely high frequency testing can be restricted to a high vacuum, high Q, low input magnitude testing environment to relax this excessive specification.) The highest resonance frequency targeted for this research is 10 MHz, and the lowest is 340 kHz, so the passband of the circuit should match or exceed these limits.

The circuit actually fabricated for these chips is more modest: it provides enough gain while introducing little enough additional noise that a detectable signal emerges from the chip. Instead of interfacing directly to test equipment, the MEMS chip output signal passes first through a series of amplification and common-mode-rejection stages. The on-chip circuit, based on the topology described previously [12] and shown in Figure 3-8, has a simulated gain of about 80. The on-chip preamplifier bandwidth, at 2.1 MHz, is also smaller than the intended bandwidth, but the fabricated MEMS devices also fell short of the planned range, so that limitation is actually a benefit in limiting noise and interferer bandwidth. For now, with the additional off-chip amplification, the on-chip preamplifier is entirely adequate.

The on-chip preamplifier is basically a differential voltage amplifier, although the subthreshold bias transistors do pass some current, so the system as a whole behaves a little like a transimpedance amplifier. The input impedance of the circuit is not yet well understood, and so backing out the MEMS output node voltage and mechanical vibration amplitude cannot yet be done with confidence: only qualitative assessments can be made at this point.

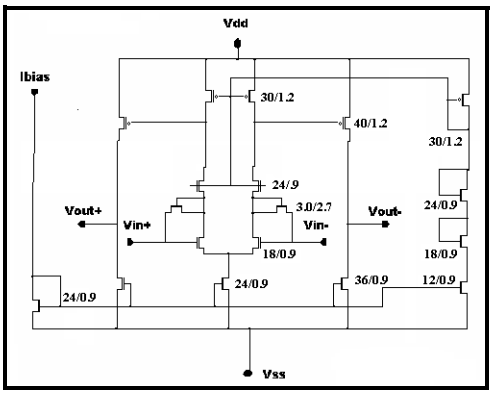

Figure 3-8. Differential amplifier with subthreshold-biased transistors biasing the inputs. The W/L ratios for the transistors are shown beside the transistors, with only one of each differential pair labeled.

4 Experimental results

The bulk of the experimentation discussed here will be the results of an intensive examination of a single device. This device is a cantilever with an electrode on the end, the topology discussed at length in the previous chapter. However, over the course of the two years of this research, six chips were laid out, fabricated, and postprocessed, containing dozens of different resonator and filter designs and a stunningly large number of individual devices. These devices also promise more results, some of which have already been gathered and are discussed at the end of this chapter.

4.1 Device 6

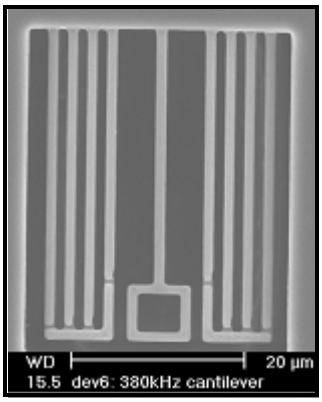

Figure 4-1. SEM of Device 6.

An SEM of one of the differential structures of Device 6, the subject of most of this chapter, is shown in Figure 4-1. The name arises from the location of the device on the chip: it is the sixth device from the left. It was designed in the TSMC .35 µm process by Jay Brotz in the third fabrication run for this research. Each device is composed of two resonator structures. The on-chip preamplifier circuit which they drive reads their electrical outputs differentially. To achieve a differential MEMS device, either the two resonators are driven so that their mechanical vibration is 180 degrees out of phase but their electrical outputs have the same phase relation to their vibration phase, or they are mechanically in phase, but their output signals have the opposite relation to their mechanical vibrations.

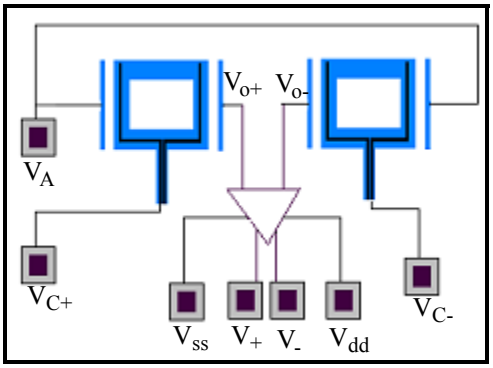

Figure 4-2. Electrode configuration for Device 6. The fixed drive electrode signal, labelled the V_A electrode, is shared by the two structures. The moving part of each resonator is driven with a single signal fed to both input and output electrodes, here labeled V_{C+} and V_{C-} for the two structures. These nodes can be driven with any of the signals described in Table 3-2 on page 41. The outputs are fed to the differential amplifier before being routed to the output pads.

Device 6 shares inputs with five other devices to reduce bondpad count and area. The electrode configuration is shown in Figure 4-2. This device was originally

designed for low-frequency testing of damping. All the conductive layers of the moving structure are connected together, so both the drive and sense electrodes share the same signals. This configuration is less than ideal for high-frequency mixer testing, as discussed in section 3.4.2, but the device has proven simple to release successfully and is an excellent device for initial testing of CMOS MEMS resonators.

Table 4-1 lists the drawn dimensions for the structure, as well as some of the predicted mechanical characteristics. The measured dimensions (from an SEM) of one device are also listed. The predicted mechanical characteristics are recalculated for the measured dimensions and also shown in the table. The thickness was not measured.

To combat the effects of vertical curling due to residual vertical stress gradients from the different temperature-dependent expansion rates of the silicon, silicon dioxide and metal layers, the cantilever beam is flanked on both sides by electrodes supported by similar cantilevers. The lengths and widths of the electrode supports are drawn identically to the length and width of the resonator. The horizontal beam seen in the bottom left of Figure 4-1 joins four cantilevers together to form the input electrode support, stiffening the four cantilevers without significantly altering their curl. The same is done for the output electrode. In this way, the resonant frequency of the input and output electrode structures is brought much higher than the resonator itself.

The curl-matched electrodes are wired to two signals. Most parts of the electrode support are grounded to minimize electrical interaction with the cantilever beam as much as possible. The part of the innermost cantilever which runs parallel to the resonator electrode is wired to the appropriate electrode signal. The electrode signal passes through the horizontal beam to the outermost cantilever, where it runs on a lower metal layer into the anchor.

These chips were processed entirely by Jay Brotz. Appendix 2 describes the processing. The generous gaps between the electrodes and the large fields of open space around the cantilever beam and electrode permit easy release of the mechanical structure.

Table 4-1. Characteristics of Device 6. The final column contains the hand calculated predictions for key characteristics based on the measured dimensions. All the hand calculations use an estimated composite Young's modulus of 62 GPa and an estimated density of 2496 kg/m^3. The effects of electrostatic spring-softening and capacitive spring stiffening are also predicted for the case where V_A=23 V, V_{C+}=23 V + $V_{C+,ac}$, V_{C-}=23 V + $V_{C-,ac}$, and V_{o+} and V_{o-} have a DC bias of V_B=1 V, obtained from Cadence simulations of the extracted layout. The capacitive load used is 378 fF to ground, also extracted from the layout.

	Drawn/Predicted	Measured/Predicted for measured dimensions
Dimensions	thickness: 3.52 μm beam width: 1 μm cantilever length: 32.3 μm electrode length: 7 μm electrode width: 1 μm drive gap: 1.55 μm sense gap: 1.5 μm	thickness: not measured beam width: 1.25 μm cantilever length: 32.5 μm electrode length: 7.28 μm electrode width: 1.25 μm drive gap: 1.25 μm sense gap: 1.25 μm
Resonator natural frequency	339,960 Hz at Vgap=0 334,600 Hz at V_p=23	418, 300 Hz at Vgap=0 412,060 Hz at V_p=23V
Mechanical spring constant	1.19 N/m	2.26 N/m
Effective mass	2.61x10^{-13} kg	3.27x10^{-13} kg
Damping in air	3.09x10^{-9} N-s/m	3.19x10^{-9} N-s/m
MEMS output electrode capacitance	drive: 0.141 fF sense: 0.145 fF	0.181 fF
Electrostatic spring constant at Vp=23	.037 N-s/m	.067 N-s/m
DC Pull-in voltage	73.9 V	99.8 V
Predicted Q in air	35	52

4.2 Electrical testing

4.2.1 Test Setup

Each MEMS chip is glued with silver paste directly to a custom printed circuit board (PCB), a schematic for which is shown in Figure 4-3. Its pads are then wirebonded with gold wire to 20-mil-wide PCB pads. The PCB provides power, ground and bias current for the on-chip pre-amplifier, as well as the MEMS signals: the V_A and V_C voltages. The PCB routes the differential outputs of the pre-amplifier to an instrumentation amplifier with a gain of 40 to 1000. Resistors determine the gain and can be changed as needed by the device under test. The amplified signal is then available for direct measurement on a BNC connector and is also fed to a mixer. The mixer's

other input is from another BNC connector, permitting connection to the V_A or V_C sources, perhaps with additional off-board processing. A differential amplifier converts a single-ended AC input to a differential V_C for the MEMS chip, providing a DC offset at the same time, if required. All the connections from the PCB to external equipment are through shielded BNC or DB25 cables. The entire PCB can be put in a vacuum chamber, with BNC and DB25 feedthroughs to the external source and test equipment.The PCB has separate ground connections for the MEMS chip and all the other ICs, so that the offset between IC ground and MEMS ground can provide the polarizing voltage.

Figure 4-3. Test PCB, showing the MEMS chip in the lightly shaded box. The circles are BNC connectors. Resistors marked by the '?' symbol select the routing path useful for the particular test.

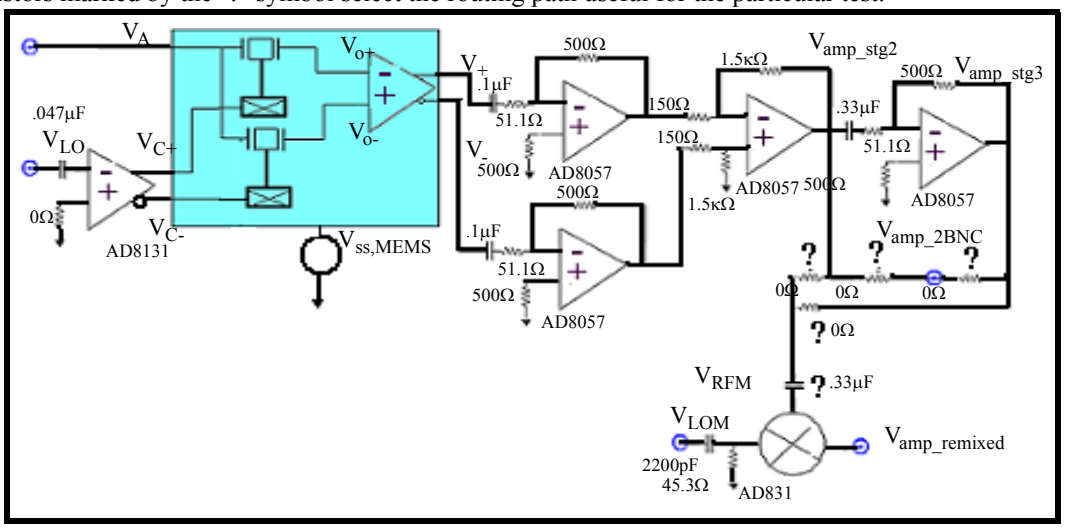

The first tests were done by driving the mixer directly with its fundamental resonance frequency. The moving electrodes on the resonator, V_{C+} and V_{C-}, drive the structures at the fundamental. The test setup for this method is shown in Figure 4-4. Note that the polarizing voltage is now on the moving structure. If the V_A electrode is also set to the polarizing voltage, the resonator can now be modeled as a one port device, with the input force appearing across the sense capacitor. Alternatively, the V_A DC voltage can be set very far from the resonator DC voltage, so that the primary force component appears across the V_A/V_C capacitor.

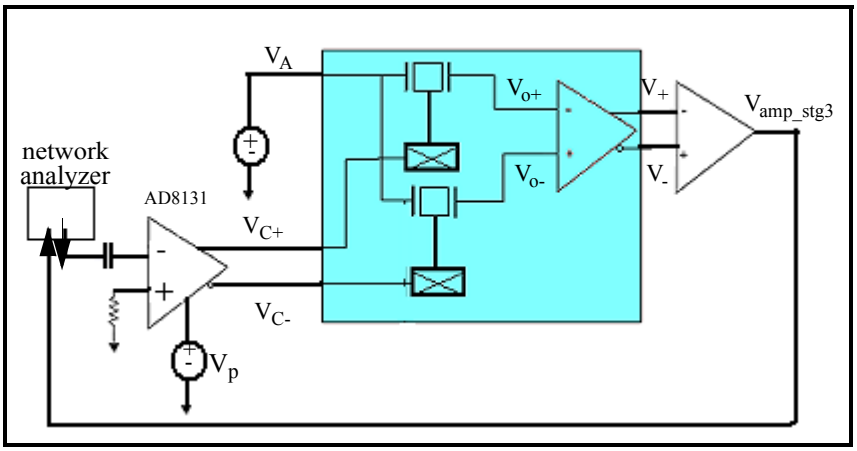

Figure 4-4. Testing differentially at the fundamental, with an external IC converting the network analyzer output to a differential signal.

The second major set of tests uses the MEMS device as a mixer-filter. When testing with the network analyzer, mixing requires a second, reference mixer to bring the MEMS output frequency back to the network analyzer's operating frequency. To make the two resonators of a differential device resonate 180 degrees out of phase, a single-to-differential converter is used to convert the network analyzer output to a differential signal which can be applied to the V_C terminals. The polarizing voltage is an offset between the ground of the external ICs and the MEMS chip. A function generator connected to the single-to-differential converter and then to the V_c electrodes outputs a fixed offset frequency, f_0. The network analyzer then sweeps over a frequency range, the center of which is $f_0 + f_r$, where f_r is the resonance frequency of interest. The MEMS mixer mixes and downconverts to the resonance frequency. The external reference mixer multiplies the MEMS output signal with the function generator signal, regenerating the network analyzer output frequency, $f_0 + f_r$. Figure 4-5 shows the test setup for mixing and using a network analyzer.

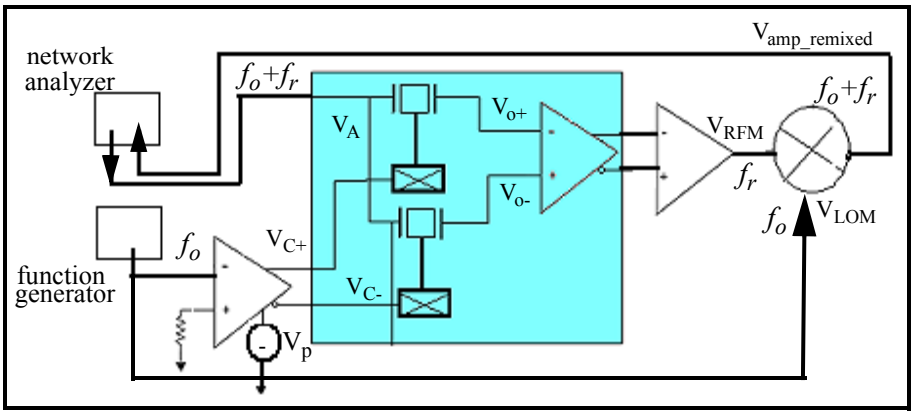

Figure 4-5. Testing mixing with a network analyzer. .

A third test setup uses the MEMS device to mix, but reads the output with a spectrum analyzer. This is the setup allowing for the most thorough characterization of the device. This setup requires two function generators, one connected through the single-to-differential converter to the MEMS device V_C inputs, and the second to the V_A input. The V_C function generator is set to a fixed offset frequency, as before. A controlling computer sets the V_A function generator to a frequency slightly below $f_0 + f_r$, and cap-

tures the spectrum output from the MEMS mixer. The computer then increments the V_A frequency slightly, and captures the new output spectrum. The controller continues to raise the frequency, saving the spectrum for each test with a new V_A frequency. This removes the effects of the off-chip mixer and captures frequency components anywhere desired in the spectrum, enabling distortion testing and thorough stopband rejection analysis. It also cuts down on feedthrough, as the measured frequency is not present in any of the sources.

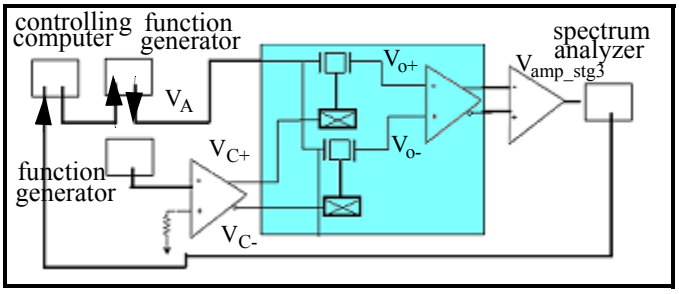

Figure 4-6. Testing mixing with a spectrum analyzer.

4.2.2 Test results for driving at the fundamental

The first tests of Device 6 were performed in air. Figure 4-7 shows the frequency response curves collected from an HP 4395A network analyzer in the test setup described in Figure 4-4. V_A was set to 3.3 V. (The original PCB terminated the V_A input with a resistor to ground, which is quite unnecessary for DC and low-frequency testing. A re-test should be performed with the V_A electrode set to the DC potential of the V_c terminals.) Opposing forces arise across the V_A-resonator capacitor and the output-node-resonator capacitor, with the net force proportional to the difference between the V_A potential and the V_o DC bias rather than V_p. The output node bias point, from simulation of the extracted circuit in Cadence, is expected to be approximately 1 V.

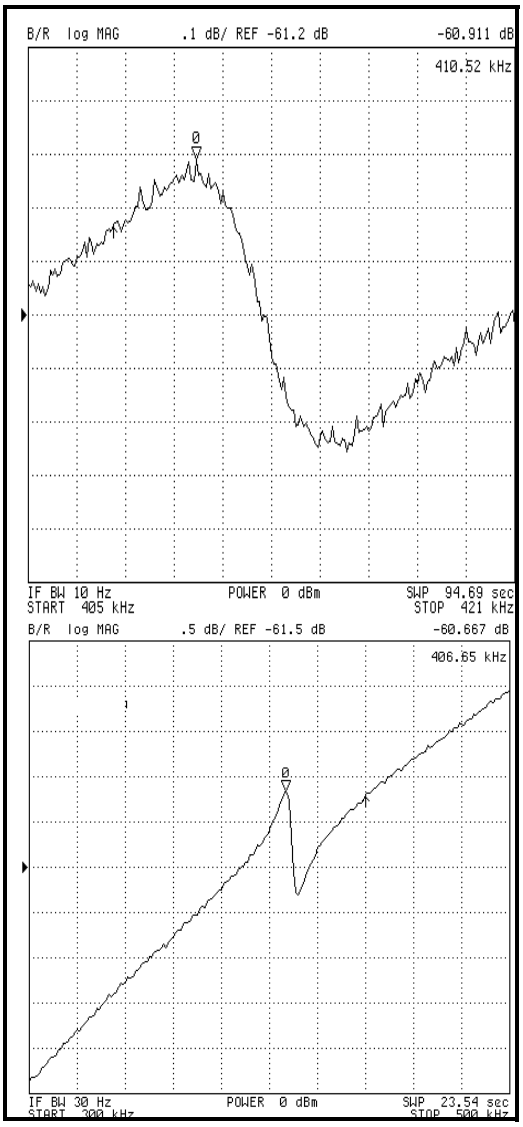

Figure 4-7. Direct drive testing at the fundamental. In a) V_p is 15 V, and the resonance frequency is 410.52 kHz. In b) the polarizing voltage has been raised to 23 V, increasing the output magnitude while decreasing the Q and the resonance frequency, which is now 406.65 kHz.

The resonance frequency of the observed transfer function in Figure 4-7 is well within the range predicted by hand calculations. A very simple upper limit for the frequency to expect can be set by finding the resonant frequency of the drawn resonator with the resonator width expanded by the expected worst-case mask misalignment of .2 μm, leaving all the other dimensions the same. Such a misalignment results in a resonant frequency at V_p=15 V of 413.7 kHz, according to the calculations presented in the previous chapter. The observed resonance frequency is 410.5 kHz.

The output signal magnitudes at resonance in Figure 4-7 are barely larger than the "stopband." In part a), the polarizing voltage is 15 V, and the peak magnitude is -60.911 dB, just a few tenths of a dB above the feedthrough level. For part b), with a higher polarizing voltage of 23 V, the peak magnitude is now -61.5 dB, about .8 dB above the feedthrough power level. As discussed in section 2.4.2, the current at the output node is the sum of the signal current, which is due to the changing MEMS capacitance at the output node, and the feedthrough currents from all the parasitic capacitances. In this test setup, the driving signal is on the output electrode and feeds through directly across the MEMS sense capacitor as well as through additional parasitic paths. The feedthrough current has not previously been added to the signal current to find the net transfer function. We do that now.

Figure 4-8 shows the electrical connections under consideration. The feedthrough current from the V_C signal on the resonator electrode to the output node, summed with the MEMS motional current, must equal the current through the parasitic capacitance to ground, giving the equation:

$$\frac{(V_p - V_{oB})C_s}{g_{0s}} sX(s) - s(C_f + C_p)V_o = -sC_f v_{lo} \qquad \textbf{(4-1)}$$

Here, C_f is the feedthrough capacitance from the V_C source to the output node. V_{oB} is the DC bias point of V_O. Following the same procedure used in Chapter 2 to arrive at Equation 2-18 on page 22, we find first the electrostatic force acting on the resonator at the primary vibration frequency, which is the sum of the V_A-side force and the V_O-side force.

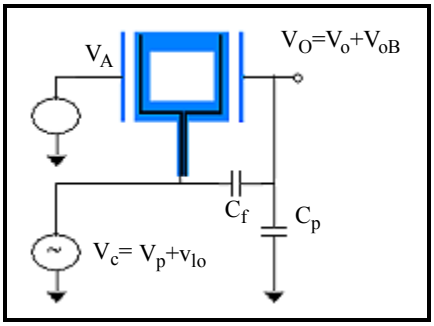

Figure 4-8. Diagram of electrical connections modeled in Equation 4-1.

We assume that the dimensions of the drive and sense MEMS capacitors are identical, with a nominal capacitance of C_s. Then we find the sum of forces, including only terms at the primary vibration frequency, as before:

$$\left(ms^2+bs+k-\frac{(V_p-V_{RF})^2C_s}{g_0^2}-\frac{(V_p-V_{oB})^2C_s}{g_0^2}\right)X+\left(-\frac{(V_p-V_{oB})C_s}{g_0}\right)V_o=\frac{(V_A-V_{oB})v_{lo}C_s}{g_0} \qquad (4\text{-}2)$$

Solving the linear system:

$$V_o(s)=\frac{v_{lo}C_f\left(ms^2+\left(b+\frac{C_s^2(V_p-V_{oB})(V_p-V_A)}{g_0^2(C_f+C_p)}-\frac{C_s^2C_p(V_p-V_{oB})(V_A-V_{oB})}{g_0^2C_f(C_f+C_p)}\right)s+k+k_e\right)}{(C_f+C_p)(ms^2+bs+k+k_e)} \qquad (4\text{-}3)$$

where the new k_e, now the sum of the spring softening across the two MEMS capacitors and the spring hardening from the output parasitic capacitor, is:

$$k_e=-\frac{C_s}{g_0^2}\left[(V_p-V_{oB})^2+(V_p-V_A)^2-\frac{C_s(V_p-V_{oB})^2}{C_f+C_p}\right] \qquad (4\text{-}4)$$

The effect of the feedthrough current, seen by comparing Equation 4-3 to Equation 2-19 on page 22, explains the zeroes seen in the measured transfer functions. At some frequency, the signal current, which makes a 180 degree shift in phase as the frequency rises from DC past the resonant frequency, becomes equal in magnitude but opposite in phase to the feedthrough current. The zero frequency can be moved to either side of the resonant peak by changing the polarity of the output voltage, accomplished by changing the polarity of V_p. Placement of the zero may eventually prove useful in improving the filter shapes for more complicated multi-resonator filters.

Because of the forces acting in opposite directions on the V_A and output nodes, the net force acting on the resonator is not proportional to V_p, but the output electrical signal is roughly linearly proportional to V_p at the resonant frequency. This indicates that to raise the output magnitude above the feedthrough, we can simply increase the polarizing voltage. However, at the same time that the output voltage magnitude rises with increasing V_p because of the larger changing electric field at

the output node, the mechanical quality factor of the resonator drops because of the larger spring softening. The resonance frequency drops as well. The slight rise in magnitude and drop in resonance frequency that accompany a change in V_p from 15 V to 23 V can both be seen in Figure 4-7. Figure 4-9 compares the output voltage transfer function of Equation 4-3, with an added feedthrough capacitance of 10 pF, for three values of V_p and the nominal dimensions of Device 6. The graph shows a case in which the polarizing voltage has been made so large that, rather than improve the output magnitude, it has instead so degraded the Q that there is no longer any resonant peak, and the resulting transfer function is a low pass filter.

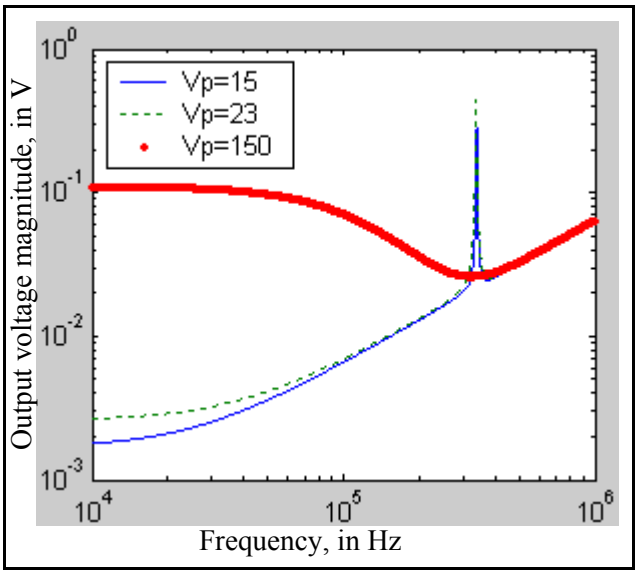

Figure 4-9. Modeling equations for the differentially driven system described, with the polarizing voltage set to 15, 23 and 150 V. The pull-in voltage for this device is about 100 V (and confirmed to be in this general range on previous chips), so the third curve couldn't be tested, but it shows the effect on the selectivity of increasing the polarizing voltage. In these equations, the V_A voltage is 3.3V, the V_C AC magnitude is 1V, and the feedthrough capacitance is 10 pF.

Equation 4-2 through Equation 4-4 simplify the system: there are additional parasitic capacitances linking the V_C signal to many other nodes in the chain of amplifiers and mixer between the MEMS output node and the input to the network analyzer.

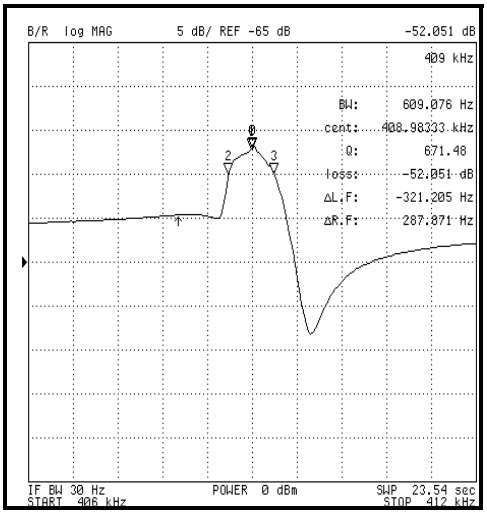

Figure 4-10. Device 6, driven differentially by an LO signal at its fundamental, tested at 1.25 Torr.

Figure 4-10 shows this same device and test setup, operated at a pressure of 1.25 Torr. The polarizing voltage remains at 23 V. Device 6 under these conditions has a Q of 671, a resonance frequency of 409 kHz, and a 3-dB bandwidth of 609 Hz. As previously discussed, in air, we expect squeeze-film damping to dominate over all other damping sources. The decrease in pressure (ambient air pressure here is measured at 720 Torr) raised the output signal magnitude without affecting the stopband magnitude, which remained at about -60 dB, as expected. The lower damping level raised the resonance frequency and both the mechanical and electromechanical Q, as predicted (as in Equation 2-20 on

page 22 and Equation 2-22 on page 22.) The local stopband around the resonant frequency is still less than 10 dB below the peak, so feedthrough may still be considerably distorting the mechanical quality factor.

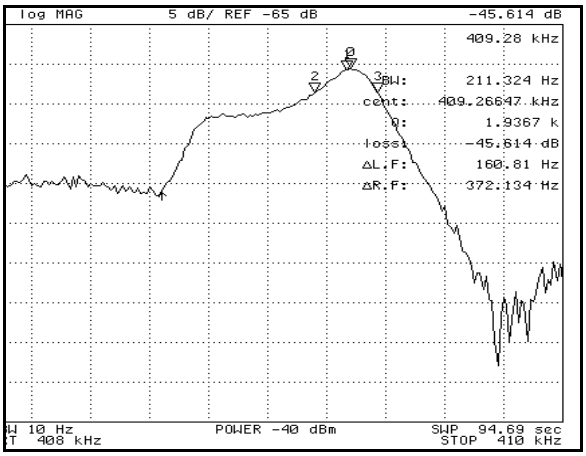

Figure 4-11. Device 6, driven differentially at the fundamental, at 207 mTorr with a 23 V polarizing voltage.

Lowering the pressure still further to 207 mTorr results in a further improvement in Q and rise in resonant frequency, bringing the output magnitude about 15 dB above the -60 dB stopband. Figure 4-11 shows the measured transfer function at this pressure with the same 23 V polarizing voltage. The transfer function is now visibly more complicated than the simple single-resonator systems discussed to this point. Two poles are visible: a larger one at 409.28 kHz, and a second about 200 Hz lower. The rise in quality factor has sharpened the passbands of the two distinct structures which form the differential device enough so that two separate poles have emerged. The measured Q of nearly 2000 then is not the Q of a single resonator. Instead, it is a measure of a structure more like a bandpass filter, composed of two sub-resonators, with a wider passband than a single resonator could provide. The minor process variations that distinguish the two resonators of Device 6 have, unintentionally, created a two-conjugate-pair-pole bandpass filter.

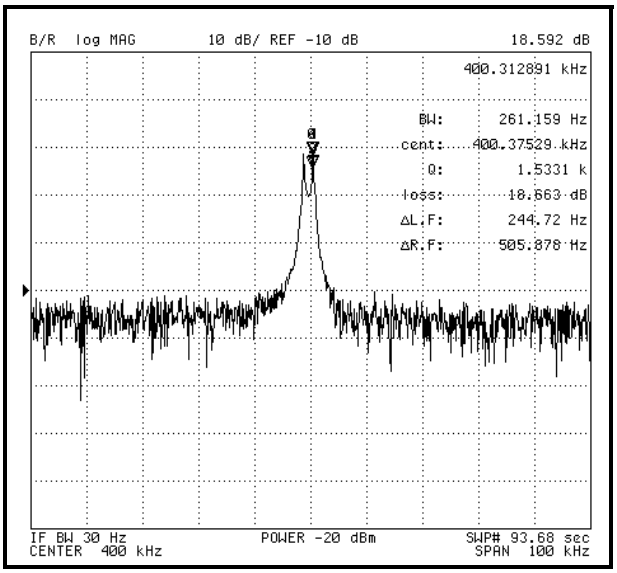

Figure 4-12. A bandpass filter constructed from the two resonators of a single differential device, operated at 8 μTorr. The individual peaks of the filter shape have quality factors of about 1500.

A second bandpass filter, also constructed from the two resonators of a single differential device, is presented in Figure 4-12. This measurement was taken in deep vacuum: 8 μTorr. For this test, the V_A electrode was set to the same potential as the V_C electrodes' DC voltage. The V_C AC magnitude was 31.6 mV. A polarizing voltage of approximately 24 V was placed on the output node by offsetting the MEMS chip's ground by 23 V. (As mentioned previously, this assumes the DC bias of the output node is 1 V.) This two-conjugate-pair pole filter has a peak gain of nearly 20 dB, a stopband

rejection of more than 20 dB, and a ripple of 8 dB, or 37%. It does not meet the specifications for the ultimate goal of this development process, but it is very promising. Again, the measured Q of 1.533 is not the Q of either of the individual resonators, as their transfer functions now overlap; it is expected that the resonator Q is much higher.

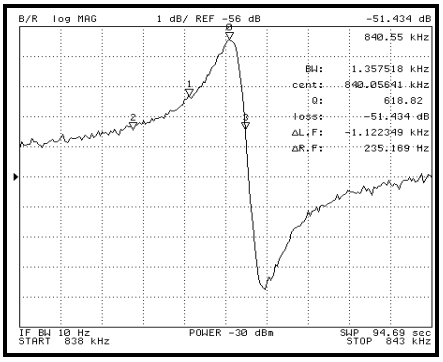

Figure 4-13. The second mode of Device 6, driven differentially without mixing, with a polarizing voltage of 23 V at 207 mTorr.

Figure 4-13 presents one last measurement of note from testing before mixing. This is a recording of the transfer function of Device 6 operating in its second resonant mode at 840.55 kHz. Except for the measured frequency span, the test conditions are the same as for Figure 4-11: the polarizing voltage is still 23 V and the pressure remains at 207 mTorr. The Q is quite respectable, at 618. No other peaks were found between 400 kHz and the end of the passband of the off-chip amplifiers, just above 3 MHz. The mechanical beam model developed so far does not help predict the second mode. We need a better model and more intensive testing to further explore the higher modes of the resonators. The effects of capacitive spring hardening, damping, and electrostatic spring softening may affect the higher modes differently than the fundamental, as their effects are ratioed to the mechanical spring constant, which will have changed. This observation explains why the second resonance frequency is not double the fundamental, but does not help predict the specifics. Higher modes are worth exploring as a possible way to increase the Q with the stiffer beam, but the same damping.

4.2.3 Test results for mixing

The initial mixing results come from tests using the network analyzer, as shown in Figure 4-5. To avoid over-driving the V_{LOM} input to the reference mixer, a 604 Ω resistor attenuates the connection between the waveform generator and the mixer input. This large resistor is unnecessary for lower waveform generator drive magnitudes An attenuation potentiometer accessible outside the vacuum system would be very useful. Alternatively, a perfectly-frequency-locked pair of waveform generators could replace the current one, with the first generating the signal to the single-to-differential converter that drives the V_C electrodes, and the second driving the mixer. This configuration would have the additional benefit of having an adjustable phase between V_{C+} and V_{LOM}. Figure 4-14 shows the measured frequency response for Device 6 at 1.25 Torr with a polarizing voltage of 23 V.

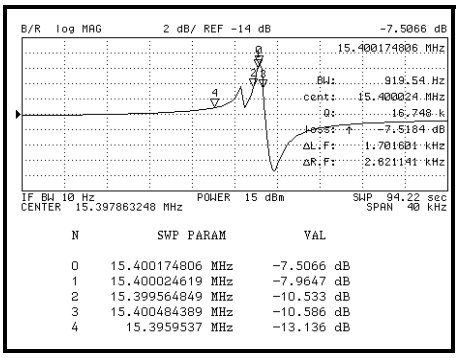

Figure 4-14. Mixing with the network analyzer at V_p=23 V, V_C at 15.000018 MHz with a magnitude of 1 V. The network-analyzer-calculated Q is incorrect, as the actual resonance frequency is lower by the V_C frequency. The Q for this resonator is 435.

The frequency response of Figure 4-14 again shows separate peaks about 200 Hz apart, underscoring that this response is more complicated than the simple biquad filter of a single mechanical resonator.

Figure 4-16 shows the output voltage transfer function of a differential pair of resonators in which a dimension of the second resonator structure is slightly skewed so it no longer perfectly matches the first. The width of the cantilever beam in the second structure has been expanded by .5 % from the nominal value for Device 6, raising the resonance frequency slightly. The transfer function is analyzed three times, with decreasing damping. Each lowering of the damping sharpens the resonant peaks and widens the distance between the phase changes of the two resonators' outputs. Eventually the peaks are far enough apart that the lower-frequency resonator phase change is sufficient to put it in phase with the output current from the second resonator, so that the differential output is no longer related to the sum of the magnitudes of the resonators' vibrations, but the difference. For this device, by this point the magnitude of the output from the first resonator is so small that its contribution to the second peak is minimal.

A disappointing observation from the graph of Figure 4-14 is that there still appears to be significant feedthrough from the network analyzer output to its input: the stopband level is still only -14 dB and the zero from feedthrough and signal cancellation is still present. Testing with the spectrum analyzer, so the vibration frequency is not present at significant levels in the sources, is necessary to separate the feedthrough effects from the mixer-filter function.

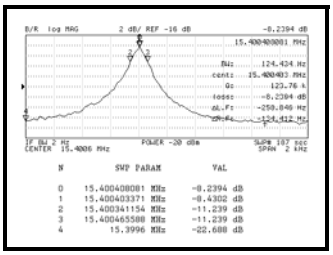

Figure 4-15. Mixing results a 8 μTorr with a V_p of 23 V and a V_C of 1 V.

Figure 4-15 shows the same device operated at 8 μTorr. The attenuation between the waveform generator and the reference mixer has been removed, and the magnitude of V_C set to 1 V. The Q from this measurement is 3229 with a stopband rejection of 14 dB. With a higher V_C to raise the signal magnitude further above the feedthrough, this should have a better Q.

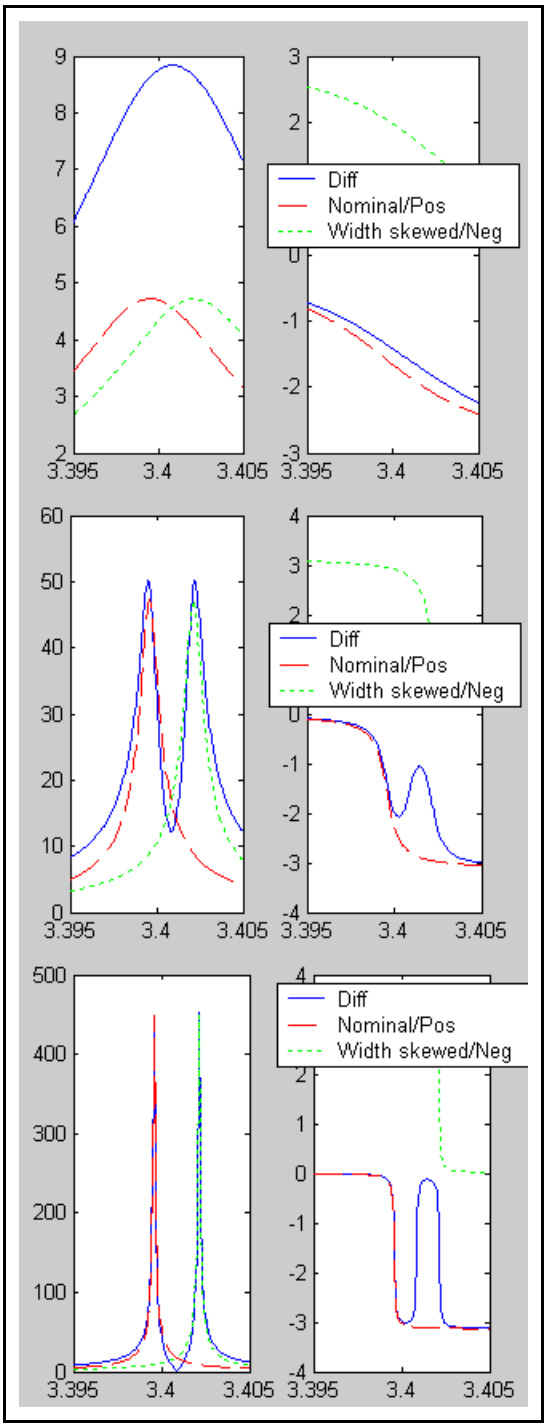

Figure 4-16. Output voltage transfer function of Device 6, in which the "positive" structure has the nominal, drawn dimensions and the "negative" structure suffers from a mask misalignment of .5 %. The transfer function used to model the individual voltage outputs is Equation 4-3 on page 51, using the voltages from section 4.2.2 and the nominal dimensions for Device 6. a) The damping factor is 1/10 the damping due to squeeze-film damping in air. The resulting differential signal is a bandpass filter with a flatter passband and sharper shape factor than either individual resonator can provide at this damping. b) The damping factor is 1/100 the damping due to squeeze-film damping in air. c) The damping factor is 1/1000 the damping due to squeeze-film damping in air.

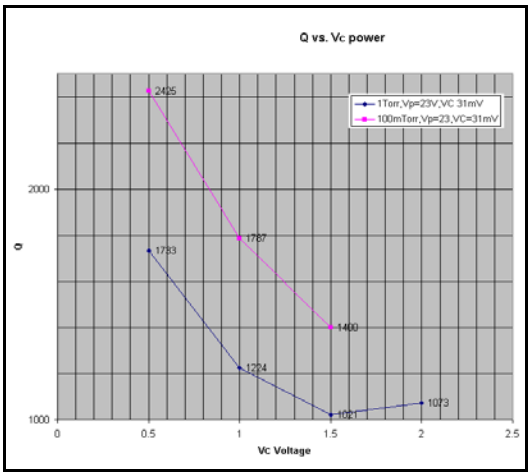

Figure 4-17. Measured Q over a range of V_A voltage magnitudes.

Figure 4-17 compares the measured quality factor over a range of pressures, V_C magnitudes and polarizing voltages and compares them to the V_A voltage magnitude. As before, the network analyzer drives the V_A electrode. To avoid over-driving the reference mixer, its input is again attenuated with a 604 Ω resistor. In the tests recorded in Figure 4-17, the waveform generator is set to output a 15 MHz sine wave with a magnitude of 1.5 V. The relation of the quality factor to the V_A voltage is as expected: Q is mostly unrelated to V_A power. The V_A voltage does have a small electrostatic spring softening effect from the component of the squared AC voltage at DC, as listed in Table 2-2 on page 15. At the maximum magnitude here, 1.5 V, for the nominal dimensions of Device 6 this would cause a voltage drop of 10.4 Hz. The rise in Q for the very small V_A voltages is probably due to noise, but worth further investigation.

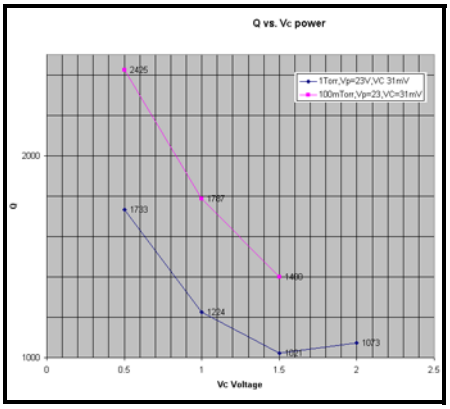

Figure 4-18. Measured Q over a range of V_C voltage magnitudes, while mixing, with Vp=23 and a V_A voltage magnitude of 31.6 mV.

The results of V_C input magnitude on the measured quality factor are shown in Figure 4-18. The apparent rise in Q as the V_C magnitude *falls* is unexpected and worthy of more investigation. In particular, this test should be repeated with a spectrum analyzer to confirm that it is not the reference mixer which is causing this effect.

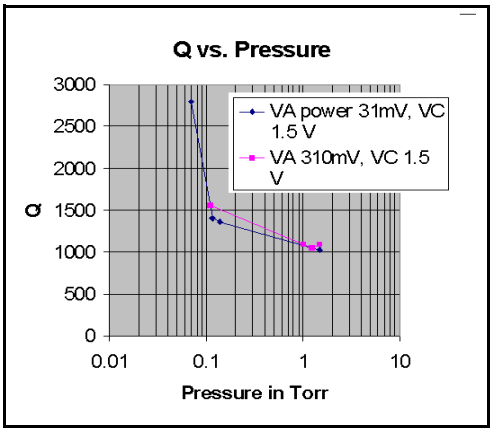

Figure 4-19. Measured quality factor is compared to the measured pressure.

Figure 4-19 shows the results of a comparison of Q to pressure. The continuing rise in Q as the pressure drops several orders of magnitude confirms that viscous gas damping is the major source of damping at the higher pressures. The Q does not rise at the same rate as the pressure falls however, so further research is also required here.

4.2.4 Other Device 6 testing

Some visual testing of Device 6 was performed by placing a packaged chip under the microscope of a Wentworth probe station and actuating a single device by directly driving it at the fundamental. An important observation from this testing is that electrode supports have their own pronounced resonance, with a Q in the same general range in air as the cantilever resonator. The V_A drive side was observed to resonate at about 1 MHz. The support was driven with a 1 MHz sine wave with a 5 V magnitude with V_C set to a DC potential of 42 V in this test.

The DC pull-in voltage of Device 6 observed in visual testing was 109 V, within the predicted range. The dimensions of the device whose actual pull-in voltage was determined were not measured. However, as can be seen in Table 4-1, the predicted pull-in voltage for Device 6 with the drawn dimensions and anticipated composite Young's modulus and density was about 75 V, whereas the pull-in voltage recalculated for the measured dimensions of one Device 6 was 99 V.

4.3 Other devices

A total of six chip designs were fabricated in the two years of this research. The first one, in the IBM SiGe 5HP process, explored basic fixed-fixed beam resonators, tuning forks, and cascades of electrostatically linked tuning forks with anticipated resonant frequencies from 1 MHz to 20 MHz. The second one, in an AMS .6 μm process, experimented further with fixed-fixed beams, tuning forks, and electrostatic coupling in the same frequency range. The next four fabrication runs were in the TSMC .35 μm process. The first of these contained a range of fixed-fixed beams and tuning forks with gaps ranging from .45 μm to .6 μm and some additional large-gap fixed-fixed and cantilever resonators designed by Jay Brotz. The small-gap devices' anticipated resonant frequencies ranged from 1 MHz to 8 MHz. The fourth run contained only fixed-fixed beams, with gaps ranging from .45 μm to 1 μm, all at 1 MHz. Half of these devices are actually composed of ganged resonators with their outputs wired together, an experiment in increasing the output magnitude. The fifth run, designed by Jay Brotz, contained additional large-gap resonators with variations on electrode design, mostly fixed-fixed beams and cantilevers. The sixth run, whose resonators were all cantilevers, experimented with variations on electrode topology, coupling mechanisms, and tuning

electrodes. The anticipated resonant frequencies for this chip design ranged from 650 kHz to 6 MHz. Table 4-2 lists these chips and their contents.

Table 4-2. Chips fabricated for resonator and filter research

Chip	Foundry Process	Resonator Topologies	Frequency Range	Drawn Gap sizes
1	IBM SiGe 5HP	Fixed-fixed beams, tuning forks, filter-cascades	1 MHz to 20 MHz	0.6 μm
2	AMS .6 μm	Fixed-fixed beams, tuning forks, filter-cascades	1 MHz to 12 MHz	0.8 μm
3	TSMC .35 μm	Fixed-fixed beams, tuning forks, filter-cascades, cantilevers	37 kHz to 8 MHz	.45 μm to 1.55 μm
4	TSMC .35 μm	Fixed-fixed beams	1 MHz	.45 μm to 1.55 μm
5	TSMC .35 μm	Fixed-fixed and cantilever beams (designed by Jay Brotz)	37 kHz-1 MHz, as calculated by Jay Brotz	1 μm
6	TSMC .35 μm	Cantilever beams, cascaded cantilevers for filters	380 kHz to 871 kHz	1.5 μm

4.3.1 Processing results

Chips 1 and 2 were processed mostly by Kevin Frederick, and partly by the author. A description of the postprocessing recipes can be found in Appendix 2. In both cases, SEMs of the resonator structures suggest that the devices have been successfully released, as Figure 4-20 shows. Chip 2 remains to be thoroughly tested.

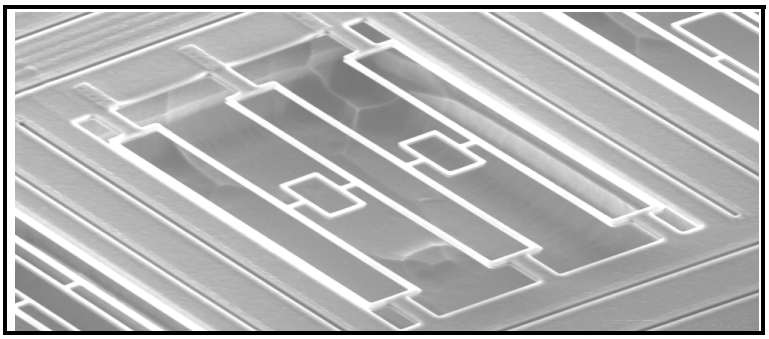

Figure 4-20. SEM of Chip 2, in the AMS .6 μm process. Note the uneven surface under the tuning fork resonator, which appears to be the substrate several microns below, indicating successful release.

The first chip suffered from electronics flaws that rendered the resonators electrically untestable. ESD clamp diodes on the MEMS inputs restricted the actuation voltages to levels useful only for very high-Q resonators, best achieved in vacuum. An utter failure of an output circuit restricted testing to visual output, an unfortunate combination our equipment could not overcome.

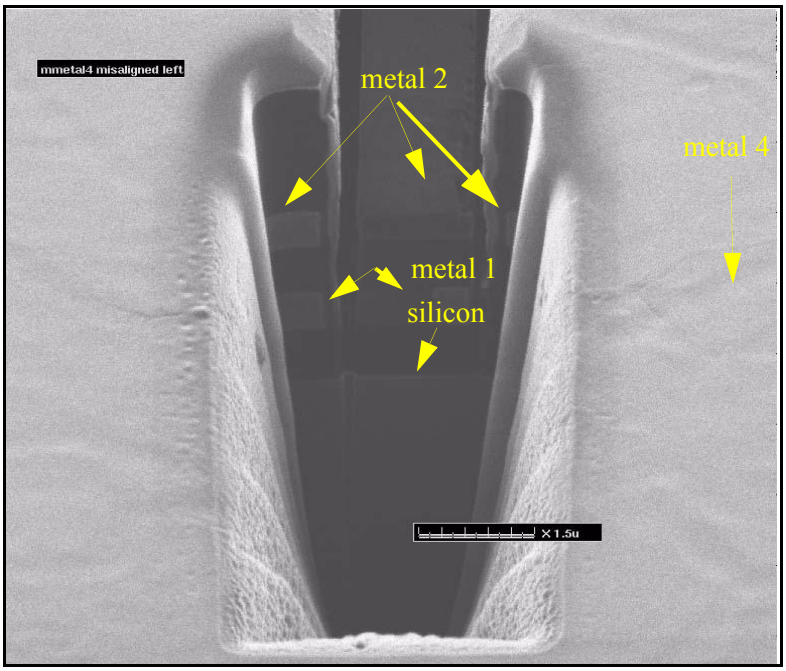

Figure 4-21. Focused ion beam image of beam 9 on the second TSMC chip. This beam, in the top center, has a drawn gap of .45 µm and a width of 1.45 µm. Its nominal height is 3.52 µm.

Unlike the resonators of the SiGe and AMS chips, the resonators of the first two TSMC chips used very aggressively sized sub-micron gaps, and unfortunately the resonator architectures did not ease the postprocessing of these small gaps with etch holes or large, nearby open areas through which etchants and by-products could easily access the gap areas. FIB exploration of the narrow gaps indicates that the oxide etch did not reach the substrate and the devices are not released. Figure 4-21 is a FIB image, taken by Jay Brotz, illustrating this problem. This is an image of a fixed-fixed beam composed of metal layers 1 and 2, with fixed electrodes to the sides topped by a protective metal 4 layers. The image is oriented towards the beam from the anchor, which has been removed. The two metal layers of the resonator, seen in the top center of the image, are clearly imaged by the ion beam, as are the two layers of the fixed electrodes to the right and left of the beam. The faint horizontal line below the lower metal layer appears to be the silicon substrate. Its distance from the metal layer indicates that it has not been etched, most likely because the oxide layer has not been completely removed in the gaps on the sides of the beam. For now, the difficulty of releasing the small-gap devices renders most of the devices on chip 3 and all of the devices on chip 4 inoperable.

The six devices with larger gaps on Chip 3 also yielded information about processing resonators. The devices are: two simple fixed-fixed beams, two fixed-fixed beams with large spaced electrodes in the center, and two cantilevers, one of which is the Device 6 described earlier. Table 4-3 lists the dimensions and anticipated resonant frequencies of these six devices.

These six devices did not inset higher metal layers in the pyramidal shape described in section 3.2. In fact, it is the observed misalignments on these devices that prompted the adoption of the pyramidal cross-section. The misalignment problem drawn schematically in part b) of Figure 3-4

on page 33 was seen in several of these devices, as shown in an SEM of an actual device in part c) of the same figure.

Table 4-3. Characteristics of the six large-gap resonators on Chip 3, as drawn. All dimensions are in μm. The Young's modulus used to predict the resonance frequency is 62 GPa and the composite density 2496 kg/m^3

Device	Type	Length in μm	Width in μm	Gap in μm	Metal Layers	Resonant Frequency	Comments
1	Fixed-fixed beam	119	1	1.5	1,2	362 kHz	
2	Fixed-fixed beam	119	1	1.5	1,3	362 kHz	Metal 2 omitted.
3	Cantilever with spaced electrode	beam:129 electrode: 7	1	drive: 1.55 sense: 1.5	1,2	36.1 kHz	Curl-matched electrodes.
4	Fixed-fixed beam with spaced electrode	beam: 57.5 electrode: 7	1	1.4	1,2	190 kHz, as calculated by Jay Brotz	Metal 2 on resonator electrode is floating on the drive side, but tied to Vp on the sense side. Metal 1 is tied to LO with a questionable via on the drive side, but floating on the sense side.
5	Fixed-fixed beam with spaced electrode	beam: 57.5 electrode: 7	1	1.4	1,2,3	190 kHz, as calculated by Jay Brotz	Metal 3 floating on drive side (LO), Metals 1 and 2 carry LO. Metals 1 and 2 floating on sense side (Vp), Metal 3 carries Vp.
6	Cantilever with spaced electrode	beam: 32.3 electrode: 7	1	drive: 1.55 sense: 1.5	1,2	340 kHz	Curl-matched electrodes.

On some released chips, the longer of the two cantilevers, Device 3, curves enough that it touches its drive or sense electrode, in some cases shorting the MEMS variable capacitor. This problem is also mostly likely traceable to a lateral mask misalignment which causes enough residual lateral stress to bend the cantilever. Experience with an entire batch of chips indicates that in fact, the mask misalignment between two adjacent metal layers may actually exceed .2 μm and additional exploration of the foundry results and the optimal cross-section is needed.

A final lesson from the mask misalignment effects on these devices is specific to the differential topology attempted in this research. In a device in which two nominally identical structures operate in parallel but with opposite phases to form a single differential device, the second structure interconnections should repeat the first, not mirror it. A mask misalignment pulling a higher metal layer to the right a fraction of a micron will have an identical effect on a repeated differential structure, but the opposite effect if the interconnection of the second device is a mirror image of the first.

4.3.2 Resonance testing

The four remaining fixed-fixed beams on Chip 3 were the subjects of visual testing. Chips were attached with silver-paste to 40-pin ceramic DIP packages and wirebonded. The packages were then breadboarded, with the necessary 15 kΩ bias resistor from the circuit bias to a 3.3 V power input. Bypass capacitors of 10 μF and 47 μF were added between the Vdd lines and ground and 1 μF and 10 μF between the bias input and ground. The breadboard was glued to a silicon wafer and placed on the vacuum stage of a probe station, where the devices were examined under a microscope.

The second device, a 119-μm-long fixed-fixed beam, was actuated with a 30 V polarizing voltage on the beam and a 5 V sine wave on the fixed input RF electrode. Motion of the beam was seen clearly at input frequencies of 1 Hz to approximately 20 Hz, with a gradually decreasing amplitude with increasing frequency. The largest vibration amplitude was at about 5 Hz. This process was repeated with a second chip, whose resonance was even more clearly observable. On the second chip, the required sine wave amplitude for clearly visible vibration was only 2.5 V, with a polarizing voltage of 10 V. The vibration was visible from 1 Hz to nearly 100 Hz. This points out a major oversight in the original design criteria for fixed-fixed structures: the need to consider residual stress, and, when necessary, to provide stress relief mechanisms in the structure.

The critical Euler buckling stress σ_E for a fixed-fixed beam is

$$\sigma_E = \frac{-\pi^2 E w^2}{3L^2}, \qquad \textbf{(4-5)}$$

where E is the Young's modulus of the material, w is the smallest dimension of the beam, and L is the largest dimension of the beam [20]. For all the fixed-fixed large-gap beams of Chip 3, the width is the smallest dimension, at 1 μm. The critical buckling stress for Device 2 of Chip 3 is approximately -14 MPa. This is not a large compressive stress value for CMOS MEMS . Clearly, stress relief of some sort is required.

5 Conclusions

The immediate goals of this research were accomplished. Electromechanical resonators were constructed from CMOS MEMS and proved to have quality factors of more than 3000 in vacuum. Very basic two-conjugate-pair-pole bandpass filters were demonstrated, with center frequency of about 400 kHz. Mixing and down-conversion with input frequencies up to 15.8 MHz proved simple, and extension to higher frequencies looks promising. A flexible test platform for direct-drive testing of resonators and filters and also for mixing and downconversion was designed and used. Guidelines for future designs of MEMS resonators, filters, and mixer-filters are proposed, as well as suggestions for improvement of the test platform.

5.1 Resonators

The resonators fabricated and tested in this research had a Q in vacuum of more than 3000. During testing, much higher Qs have been observed, and the results must be confirmed. The model developed for the resonators proved to predict their resonance frequencies and electrostatic spring softening fairly well, once the variation in dimensions due to processing variations was accounted for. Additional characterization of the Young's modulus and density for the process and layer stack will improve the predictive ability. Testing of a larger number of resonators with a larger range of tuning voltages is also necessary. Because the input impedance of the on-chip amplifier is not well-understood, the actual MEMS voltage magnitude and vibration amplitude cannot be quantitatively verified, but their behavior qualitatively matches the model.

Some additional work must be done to improve the test setup for characterizing resonators. Testing by driving with signal generators and capturing the output with a spectrum analyzer will give a much more complete and accurate picture of the behavior of these resonators. If testing is also done by mixing, it will eliminate the presence of any sources with large components at the mixing frequency. It also captures the whole spectrum of the response, including the modulation products and higher harmonics, all necessary terms to quantify in the analysis of a resonator. Most of the Labview program to manage this process with an Agilent 8395A spectrum analyzer and Agilent waveform generators is written and simply waiting to be tweaked and used.

Because of the differential design of the devices in this research, the Q of individual resonators has not yet been measured. It's essential to either separate the peaks of the two structures of a device by applying a DC offset between them, or to turn one off by not driving it or not sensing it. The transfer functions presented in this thesis all include the effects of both resonators of a differential device; it is anticipated that the measured Q of a single resonator will be somewhat higher than the combined Q of two structures whose resonant frequencies are slightly offset.

It's also necessary to better model the circuit in order to be able to back out the voltage and mechanical vibration amplitudes.

Experience with these resonators leads to a few general guidelines for CMOS MEMS resonator design.

1. Lateral residual stress, controlled by the commercial CMOS foundry used to fabricate the chips, affects the resonant frequencies of clamped-clamped structures. Rather than attempt to design resonators that are small enough that residual compressive stress does not cripple them, and to account for the effects of an anticipated stress on the resonance frequency and adapt the dimensions to compensate for it, it is more sensible to provide stress relief mechanisms in the structure. Future designs may experiment with stress-relieving anchors. A large, released plate, suspended over the substrate by folded beams or other soft springs, can act as the anchor for new fixed-fixed resonator structures. The soft support springs should reduce the residual stress of the released plate dramatically.
2. An essential part of further development of cantilever resonators is improving the drive and sense electrodes. Better alternatives to the curl-matched cantilever-supported electrodes, which now have a pronounced resonance of their own, must be developed. At the very least, more cross bars joining the cantilever supports are required to make the supports stiffer. The supports can also be placed further from the anchor's ground plane and any other metal at a different potential, so that stray forces exciting them to resonate decrease. Shorter, high frequency cantilevers may be able to do away with curl-matching altogether, especially in fairly low-stress processes.
3. It is best to make the resonator structure as large as possible, within the constraints of area limitations and curl and residual stress constraints. Larger dimensions combat the effects of process variations on the dimensions of a CMOS MEMS device. They also make the device stiffer, so the necessary tuning voltage to achieve the same frequency shift is also larger. This is actually also a benefit, because it makes the resonator more robust to voltage noise. Because of the dependence of the force on the square of the voltage across the gap, any voltage noise on the electrodes of the resonant structure appears as a spring softening term which moves the resonant frequency of the device. The larger the mechanical spring constant of the device, the smaller will be the frequency-shifting effect of the voltage noise. If the larger device also has larger transduction electrodes, its output magnitude also increases.
4. Attention to making structures easy to release is essential, particularly for the aggressively small gaps and high aspect ratios critical to achieving a large output magnitude on electrostatically actuated resonators. Large open areas and etch holes should be included near small gaps whenever possible. Continuing research in both better topologies for MEMS postprocessing and more aggressive processing attempt to solve the release problems we encountered with small gaps.

5. It is not clear that the differential sensing attempted in this research is actually beneficial. Because it is difficult to achieve perfectly matched fabricated structures, as it is difficult to achieve an extremely symmetric differential drive signal, the resonant frequencies of the individual structures tend to move apart, decreasing the system Q rather than increasing it.

Some areas in which more research is still needed, particularly in formulating additional design guidelines, are:

1. Damping mechanisms, both in air and in vacuum, are still poorly understood. With good models of damping, topologies and sizing can be better optimized for the best Q and output magnitude.
2. In a closely related spur of research, investigation of resonator topologies with lower anchor losses could greatly improve the Q of future resonators. Adaptation of free-free node-clamped beams to CMOS MEMS lateral electrodes could be a good first step.
3. The limits of CMOS MEMS postprocessing must be explored and explicitly quantified to provide design guidelines for maximum aspect ratios near minimum gaps, minimum release requirements, placement of vias, and misalignment guidelines for each foundry process used.

Some directions that look especially promising for future work are:

1. An alternative approach to creating the very small gaps essential to high quality-factor, large output resonators is to construct them after fabrication, by moving one or both of the electrode plates after release. Some experimentation has already been done with electrode plates moved by deliberately-created lateral stress during the period of research covered by this thesis, but the structures have not yet been tested.
2. Linear electrostatic comb finger sensing might be a useful subject of research, as the benefits of a linear sensing technique could be great for low-distortion MEMS filters.

5.2 Filters

Current test results demonstrate filtering at 400 kHz with a stopband rejection of 28 dB. As in the previous section, a better test setup is essential. Decreasing the response to feedthrough in the system by testing with a spectrum analyzer and driving the filters as mixers would improve the ability to test the true response of the filters.

The cantilever resonator examined here proved to be so compliant that voltage noise and small voltage offsets move the resonance frequencies of the individual resonators by 100s of Hz, a significant portion of the passband for these filters. Controlling the positions of the poles would be easier with stiffer resonators.

A topic of future research is image rejection. It may prove trickier than initially anticipated to successfully perform image rejection by replicating a differential device, driving it with 90-

degree phase shifted inputs, and summing the outputs. Because these resonators have fairly high quality factors, and the phase of their output signals reverses after passing the resonance frequency, it may prove difficult to match resonator frequencies closely enough to achieve image rejection. Again, larger resonators are one of the solutions.

Some theory has been worked out to pave the way for constructing better filters, with more resonators, better ripple and better stopband rejection. In fact, more complicated filters with several coupling mechanisms have been fabricated and are simply waiting to be tested.

5.3 Mixers

Mixing proved quite easy in the testing of these MEMS mixer-filters. No problems are anticipated in extending the frequency range up to hundreds of MHz. The testing PCB is adequate to 80 to 100 MHz for mixing and testing with the network analyzer. An even better testing setup would use the spectrum analyzer. For high-Q testing, the single-to-differential converter can be omitted and a single structure tested, rather than testing both structures of a differential device at once.

One of the disappointments in testing with the current setup, the reference mixer, and the network analyzer, is the significant feedthrough power still seen. As mentioned repeatedly, testing with the spectrum analyzer promises to be a much better approach.

There are two other major problems with the current mixing test setup using the network analyzer. First, the phase of the V_{LOM} signal input to the reference mixer cannot be independently adjusted relative to the phase of the V_C inputs to the MEMS device. The phase of this signal relative to the downconverted output of the MEMS device, the second input to the reference mixer, is absolutely critical to the magnitude of the re-mixed output. The current setup most likely does not give an accurate reading for the output magnitude from the system because of this flaw.

The second major problem with the current test setup is that the magnitude of the V_{LOM} is linked to the magnitude of the V_C signals. Either the magnitude of all is restricted to less than 1V, the upper limit for the external reference mixer—not a good solution, as we would like to be able to drive the mixer-filter harder—or an attenuator must be inserted between the signal source and the reference mixer input. In practice, the second solution has been used so far, with a single resistor providing the attenuation. The attenuation level should change with each change in the magnitude of $V_{C,}$ but in practice, because that would require turning off the vacuum system, opening it and replacing the resistor, that hasn't been done. Instead, the magnitude of the mixer input drops from a maximum of just less than 1 V for a 6 V signal to the MEMS device to about 160 mV for a 1 V

signal to the MEMS device. For these small magnitudes at the mixer, the mixer introduces unnecessary attenuation of the output signal at the operating frequency to the network analyzer.

Bibliography

[1] http://www.nec.co.jp/press/en/0110/0402.html

[2] http://www.chipcenter.com/analog/products_700-799/prod793.htm

[3] K. Wang and C. Nguyen, "High-order medium frequency micromechanical electronic filters", *J. Microelectromechanical Systems*, vol. 8, no. 4, Dec. 1999, pp 534-556.

[4] S. No and F. Ayazi, "The HARPSS process for fabrication of nano-precision silicon electromechanical resonators", *Proc. of IEEE-Nano 2001*, Oct. 2001, pp 489-494.

[5] A. Abidi, "Direct-conversion radio transceivers for digital communications", *IEEE J. of Solid-State Circuits*, vol. 30, no. 12, Dec. 1995.

[6] G. K. Fedder, S. Santhanam, M. L. Reed, S. C. Eagle, D. F. Guillou, M. S.-C. Lu, and L. R. Carley, "Laminated High-Aspect-Ratio Microstructures in a Conventional CMOS Process**,"** *Proceedings of the 9th IEEE International Workshop on Micro Electro Mechanical Systems (MEMS '96)*, Page 13-18, February 15-17, 1996, San Diego, CA, USA

[7] Johnson, R., *Mechanical Filters in Electronics*, New York: Wiley-Interscience, 1983.

[8] Nguyen, C., "Micromechanical signal processors", *Ph.D. Dissertation*, Dept. of Electrical Engineering and Computer Sciences, UC Berkeley, CA, Sept. 1994.

[9] F. Bannon, J. Clark and C. Nguyen, "High Frequency Microelectromechanical IF Filters", *Proceeding of International Electron Devices Meeting,* Dec. 1996, pp 773-776.

[10] L. Lin, R. Howe, and A.P. Pisano, "Microelectromechanical filters for signal processing", *J. Microelectromechanical Systems*, Pages 286-294, Sept. 1998, vol. 7, no. 3

[11] R. Navid, J. Clark, M. Demirci, et al., "Third-order intermodulation distortion in capacitively-driven CC-beam micromechanical resonators", *14th International IEEE Conf. on MEMS*, Jan. 2001, Interlaken, Sweden, pp. 228-231.

[12] H. Luo, "Integrated multiple device CMOS-MEMS IMU systems and RF MEMS applications", *Ph D. Thesis*, Dept. of Electrical and Computer Engineering, Carnegie Mellon University, Dec. 17, 2002.

[13] Q. Jing, H. Luo, T. Mukherjee, et al., "CMOS micromechanical bandpass filter design using a hierarchical MEMS circuit library", *Proceedings of 13th International IEEE Conf. on MEMS*, Jan. 2000, Miyazaki, Japan, pp. 187-192

[14] S. Pourkamali, R. Abdolvand and F. Ayazi, "A 600 kHz electrically-coupled MEMS bandpass filter", *Proceedings of 16th International IEEE Conf. on MEMS*, Jan. 2003, Kyoto, Japan, pp. 702-705.

[15] D. Galayko, A. Kaiser and L. Buchaillot et al., "Microelectromechanical variable-bandwidth IF frequency filters with tunable electrostatical coupling spring", *Proceedings of 16th International IEEE Conf. on MEMS*, Jan. 2003, Kyoto, Japan, pp.153-156.

[16] K. Wang, A.-W. Chong, C. Nguyen, "VHF free-free beam high-Q micromechanical resonators", *J. MEMS*, vol. 9, no. 3, Sept. 2000.

[17] X. Huang, M. Prakash, Ca. Zorman, et al. "Free-free beam silicon carbide nanomechanical resonators", *Proceedings of 12th International Conference on Solid State Sensors, Actuators and Microsystems*, June 2003, Boston, pp. 342-343.

[18] J. Wang, Z. Ren, C. Nguyen, "Self-aligned 1.14-GHz vibrating radial-mode disk resonators", *Proceedings of 12th International Conference on Solid State Sensors, Actuators and Microsystems*, June 2003, Boston, pp. 947-950.

[19] E. Quevy, B. Legrand, D. Collard et al., "Ultimate technology for micromachining of nanometric gap HF micromechanical resonators", *Proceedings of 16th International IEEE Conf. on MEMS*, Jan. 2003, Kyoto, Japan, pp. 157-160.

[20] S. Senturia, "Microsystem Design", Boston: Kluwer Academic Press, 2001.

[21] H. Xie, "Gyroscope and micromirror design using vertical-axis CMOS-MEMS actuation and sensing", *Ph.D Thesis*, Dept. of Electrical and Computer Engineering, Carnegie Mellon University, 2002.

[22] S. Diamantis, M. Ahmadi, G. Jullien et al., "A programmable MEMS bandpass filter", *Proc. 43rd Midwest Symp. on Circuits and Systems*, Aug 2000, Lansing, MI, pp. 522-525.

[23] H. Baltes, O. Paul, J. Korvink, "Simulation toolbox and material parameter database for CMOS MEMS", *Proc. 7th International Micro Machine and Human Science Symposium*, Oct. 1996, pp. 1-8.

Appendix 1: Matlab code for effective mass

```
function mstuff=cantileverEffM(rho,w,h,l,we,he,le)
%function mstuff=cantileverEffM(rho,w,h,l,we,he,le)
%returns info about the effective mass of a cantilever with a square
%electrode on the end to which a point force is applied. mstuff is
%an array of [(total mass of the cantilever beam) (effective mass of cantilever)
%(effective mass/total mass for cantilever) (mass of electrode)
%(total effective mass of cantilever +electrode)]
%rho--material density in kg/m^3
%h---thickness in um (all the rest in um)
%l--length
%w--width
%we--width of the electrode
%he--thickness of the electrode
%le--length of the electrode
l=l*1e-6;
w=w*1e-6;
h=h*1e-6;
le=le*1e-6;
he=he*1e-6;
we=we*1e-6;
mbeam=rho*w*h*l;
%the ratio of the effective mass of the cantilever beam to the real mass
%of just the cantilever beam
mr=(le^2*l^2/80+13*le*l^3/360+11*l^4/420)/((l^2/3+le^2/4+l*le/2)^2);
meffbeam=mr*mbeam;
%find the effective mass of the first crossbar of the electrode head.
%it's rho*le*h/yref^2*Int((y(l)+ y'(l)*(x-L))^2)dx.
yref=l^3/3+l*le^2/4+l^2*le/2;
meffxbar1=rho*le*h/yref^2*intyx2(l,le,0,we);
%find the effective mass of the two crosspieces that make the electrode
%plate, minus the widths of the end and start crossbars.
meffplate=rho*we*h/yref^2*intyx2(l,le,we,le-we);
meffxbar2=rho*le*h/yref^2*intyx2(l,le,le-we,le);
meffhead=meffxbar1+2*meffplate+meffxbar2;

mefftotal=meffbeam+meffhead;
mstuff=[mbeam meffbeam mr meffhead mefftotal];
```

Appendix 2: CMOS MEMS postprocessing recipes

This recipe is from Jay Brotz, who did all the processing on the chips containing Device 6. It is adapted from recipes used for earlier chips by previous students in the CMU ECE MEMS Lab.

CMOS MEMS Post-Processing Details

1. Clean
    a. Wash chips in beaker of acetone for 5 minutes with ultrasonic agitation
    b. Rinse with methanol, dry
2. Oxide etch
    a. Load chips into PlasmaTherm International RIE etcher
    b. Etch: CHF_3 at 22.5 sccm and O_2 at 16 sccm, RF power 100 W
        i. Pressure 125 mTorr for 185 min
        ii. Pressure 100 mTorr for 50 min
3. Polymer residue removal
    a. Wash chips in a beaker of EKC6800 (proprietary mixture from EKC) for 60 minutes with occasional gentle agitation
    b. Rinse chips in water, then methanol, and dry
4. Carrier wafer preparation
    a. Spin AZ4210 photoresist onto a 4 inch wafer: ramp at 1000 RPM for 6 sec, spin at 1200 RPM for 30 sec
    b. Mount chips, bake at 120 degrees C for 20 min
5. Silicon etch
    a. Load carrier wafer into Surface Technology Systems Multiplex ICP DRIE etcher
    b. Anisotropic (vertical) etch: 15 minutes (75 cycles), pressure 15 mTorr
        i. Etch segment: SF6 at 130 sccm and O2 at 20 sccm, RF power 600 W on coil, 100 W on platen
        ii. Passivate segment: C4F8 at 120 sccm, RF power 600 W on coil, 0 W on platen
    c. Isotropic etch: SF6 at 130 sccm, RF power 600 W on coil, 12 W on platen, pressure 50 mTorr, 5 min
6. Unmount from carrier wafer